ACS OMEGA

Open Access

http://pubs.acs.org/journal/acsodf

Article

Design, Characterization, and Evaluation of Textile Systems and Coatings for Sports Use: Applications in the Design of High-Thermal Comfort Wearables

Ian C. Orjuela-Garzón,* Cristian F. Rodríguez, Juan C. Cruz, and Juan C. Briceño

Cite This: *ACS Omega* 2024, 9, 49143−49162

Read Online

ACCESS | Metrics & More | Article Recommendations

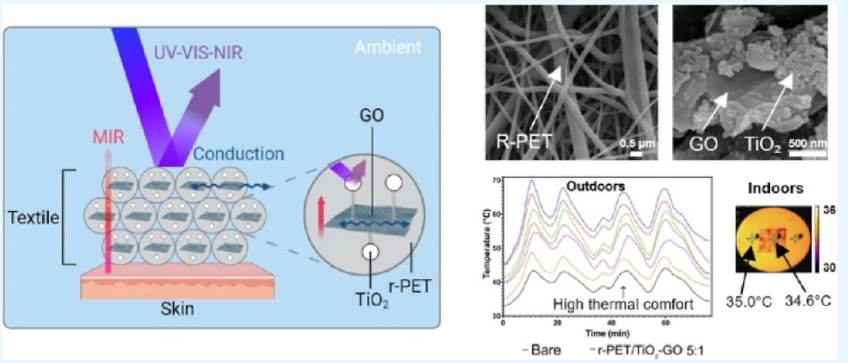

ABSTRACT: Exposure to high temperatures during indoor and outdoor activities increases the risk of heat-related illness such as cramps, rashes, and heatstroke (HS). Fatal cases of HS are ten times more common than serious cardiac episodes in sporting scenarios, with untreated cases leading to mortality rates as high as 80%. Enhancing thermal comfort can be achieved through heat loss in enclosed spaces and the human body, utilizing heat transfer mechanisms such as radiation, conduction, convection, and evaporation, which do not require initial energy input. Among these, two primary mechanisms are commonly employed in the textile industry to enhance passive cooling: radiation and conduction. The radiation approach encompasses two aspects: (1) reflecting solar spectrum (SS) wavelengths and (2) transmitting and emitting in the atmospheric window (AW). Conduction involves dissipating heat through materials with a high thermal conductivity. Our study focuses on the combined effect of these radiative and conductive approaches to increase thermal energy loss, an area that has not been extensively studied to date. Therefore, the main objective of this project is to develop, characterize, and evaluate a nanocomposite polymeric textile system using electrospinning, incorporating graphene oxide (GO) nanosheets and titanium dioxide nanoparticles (TiO_2 NPs) within a recycled polyethylene terephthalate (r-PET) matrix to improve thermal comfort through the dissipation of thermal energy by radiation and conduction. The textile system with a 5:1 molar ratio between TiO_2 NPs and GO demonstrates 89.26% reflectance in the SS and 98.40% transmittance/emittance in the AW, correlating to superior cooling performance, with temperatures 20.06 and 1.27 °C lower than skin temperatures outdoors and indoors, respectively. Additionally, the textile exhibits a high thermal conductivity index of 0.66 W/m K, contact angles greater than 120°, and cell viability exceeding 80%. These findings highlight the potential of the engineered textiles in developing high-performance sports cooling fabrics, providing significant advancements in thermal comfort and safety for athletes.

1. INTRODUCTION

The escalation of global temperatures due to climate change has increased human exposure to elevated temperatures, both indoors and outdoors.[1] Heat stress, defined as the excessive heat the body can tolerate without suffering physiological damage, becomes a critical issue when internal regulatory mechanisms fail to maintain the body's base temperature.[2] The body's primary method of heat dissipation, which involves directing up to 48% of the blood flow to the skin to facilitate perspiration, can result in decreased blood flow to vital organs, muscles, and the brain, leading to acute dehydration.[3] Consequently, there is a heightened risk of heat-related illnesses (HRIs), which can range from benign symptoms such as rashes, cramps, and heat exhaustion to severe conditions such as heatstroke (HS).

Received: June 14, 2024
Revised: October 13, 2024
Accepted: October 15, 2024
Published: November 28, 2024

Statistical data from international athletics competitions indicate an average HRI incidence rate of 11.7 athletes per 1000 participants.[4] Similar occurrences are noted in indoor sports like basketball.[5] During the Tokyo 2020 Paralympic Games, 30% of athletes reported HRI symptoms.[6] HS fatalities are ten times more prevalent than severe cardiac events in warm weather sporting events and rank among the top three causes of death in athletes,[7] contributing to 15% of annual fatalities among football athletes.[5] Untreated HS events can lead to mortality rates as high as 80%.[8]

Current methodologies to control thermal comfort include increasing heat loss in enclosed spaces and in the human body. The former is achieved through air conditioning and fans, accounting for 15% of electricity consumption and 10% of global greenhouse gas emissions.[9] The latter involves the use of advanced textile technologies to create a temperature-controlled microenvironment between the wearable system and the skin.[10,11] Heat transfer mechanisms—radiation, evaporation, conduction, and convection—between the human body and the environment facilitate thermal comfort without additional energy input.[12] The human body with clothing uses conduction as the main route of heat transport between the skin and the inner surface of textiles, as well as within the textile itself, when the environment is closed.[13]

While conduction remains a primary route of heat transport in enclosed environments, convective heat transfer also plays a crucial role, particularly in the microclimate between the skin and the textile. The presence of trapped air leads to complex temperature and humidity gradients, significantly influencing overall thermal comfort.[14] The thermal resistances due to conduction and convection are effectively connected in series, highlighting the importance of both mechanisms in the overall heat transfer process. Convective heat transfer is particularly prominent in dynamic textiles that alter their porosities in response to humidity levels. However, it is important to note that these textiles have limitations, including slow response times, high production costs, and functionality that is primarily limited to conditions involving perspiration.[14,15] Radiation significantly contributes to dry heat transfer between the textile's external surface and the environment, accounting for over 40% of total heat loss.[16]

Recent advancements in thermoelectric materials have led to the development of skin-like devices capable of both heating and cooling functions. These innovations are particularly relevant for thermal comfort applications and for creating artificial heating and cooling sensations in virtual and augmented reality (VR/AR) environments. For instance, flexible thermoelectric devices based on Bi_2Te_3/Ag flake-ecoflex/polyimide-coated Cu materials have demonstrated the ability to generate temperature differentials of up to 12 °C in wearable systems designed for both cooling and heating applications.[17] Such devices offer precise temperature control and rapid switching between heating and cooling modes, which are crucial for creating realistic thermal feedback in VR/AR applications.

While our current study focuses on passive cooling techniques, the integration of active thermoelectric elements with radiative cooling textiles presents an intriguing avenue for future research. This combination could potentially offer a hybrid solution that provides both passive daytime cooling and on-demand heating or additional cooling, as required by the user or dictated by environmental conditions. Future work could explore how to optimally combine these active and passive approaches to maximize the thermal comfort across a wide range of scenarios.

Textiles can transfer infrared (IR) thermal energy to the environment through the atmospheric window (AW), which is highly transmissive/emissive at wavelengths between 8 and 13 μm.[18−20] Similarly, the textile can reflect the wavelength range of the solar spectrum (SS) between 0.3 and 2.5 μm.[21] Research highlights the use of coatings in photonic structures, dielectrics, polymers, and composites.[22] Inorganic compounds such as silicon dioxide, vanadium dioxide, and titanium dioxide (TiO_2) exhibit excellent weather resistance, thermal stability, and chemical inertness. Notably, TiO_2 with its high refractive index, availability, biocompatibility, and low cost is advantageous for enhancing reflectance.[23]

TiO_2 nanoparticles (TiO_2 NPs) offer a larger surface area and improved reflectance due to increased boundaries compared to larger-sized elements.[24] Coating cotton textiles with TiO_2 NPs increases reflectivity in the visible (vis) and near-infrared (NIR) regions, resulting in lower temperatures compared to untreated fabrics.[25] Similarly, TiO_2 NP-coated silk textiles, using atomic layer deposition, exhibit significant reflection cooling, achieving a temperature drop of approximately 10.1 °C relative to unprocessed silk fibers.[26] Polytetrafluoroethylene coated with TiO_2 and polylactic acid achieves solar reflectance and emittance values in the AW of 0.92 and 0.95, respectively, resulting in a 4.8 °C drop in skin temperature.[27] A Janus membrane coated with TiO_2 using the radiofrequency cathodic erosion increased surface reflectance in the vis−NIR spectrum by about 90%, a temperature difference of 22 °C.[28]

Conduction cooling, mainly related to thermal energy dissipation through textile fibers,[29] utilizes conductive materials like silver nanowires, carbon nanotubes, and graphene derivatives, including graphene oxide (GO).[30] Studies demonstrate that reduced GO sprayed on a poly(vinylidene fluoride/hexafluoropropylene) substrate exhibits high sunlight absorbance, high AW transmittance/emittance (85%), and a temperature differential of 11.1 °C between fabric surfaces.[31] Selective permeation hydrogels coated with GO on nonwoven membranes show an 85% improvement in thermal conductivity.[32] Polyacrylamide membranes coated with GO, reduced GO, and iron oxide nanoparticles present a 5% increase in water vapor permeability compared to the pristine membrane.

Nanocomposites are typically incorporated into fibers for textile production. Synthetic fibers are gaining popularity for thermal comfort due to their superior washability, wearability, fast drying, and low moisture retention.[33] Polyamide, particularly polyamide 6 (PA6), and polyesters such as polyethylene terephthalate (PET) are well-known in this category.[34] PET fibers are favored for their low toxicity, high durability, strength, dimensional stability, chemical resistance, and ease of production, making it the most widely used material for fiber development and representing 52% of global fiber production.[35,36] PET-based textiles can increase the scattering and reflection of the UV−vis spectrum wavelength. Reflectance at longer wavelengths, such as those in the infrared (IR) spectrum, is minimal (with values below 0.1 in the AW). Consequently, the material's behavior in this wavelength range is primarily governed by transmission and emission processes.[37,38] This can be achieved by manipulating the fiber properties of formed films during manufacture.

https://doi.org/10.1021/acsomega.4c05600
ACS Omega 2024, 9, 49143−49162

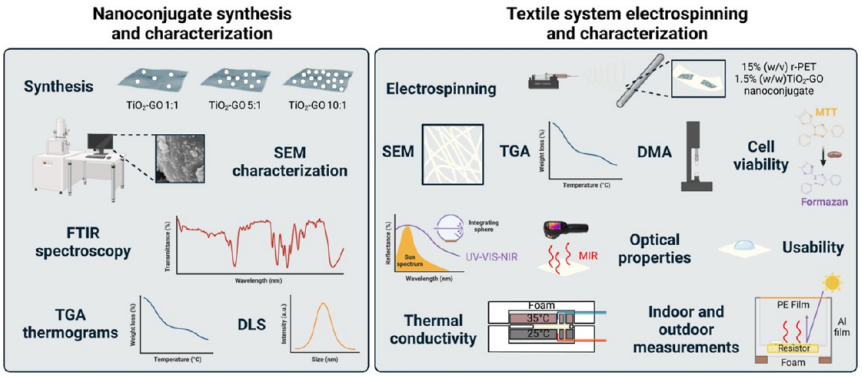

Figure 1. Workflow of elaboration, characterization, and evaluation of r-PET textile systems with GO nanoconjugates and titanium dioxide nanoparticles for thermal comfort by heat dissipation through conduction and radiation.

Various methods for producing thermally controlled textiles include miniemulsion processes, hydrothermal methods, magnetic sputtering, dip coating, electrolysis, and electrospinning (ES).[39−43] ES is widely used due to its simplicity, cost-effectiveness, ability to produce fibers from a wide variety of polymers, high surface area to volume ratio, low density, and high pore volume.[44] Recent studies have demonstrated the significant potential of electrospun nanofibers in enhancing the radiative cooling for wearable devices. The unique properties of these nanofiber networks, including their high porosity and large surface area, contribute to their effectiveness in thermal management. For instance, recent work has shown that electrospun polyethylene nanofibers can achieve remarkable cooling power of up to 550 W/m^2 under direct sunlight.[45] Additionally, composite nanofibers incorporating phase-change materials have demonstrated the ability to maintain stable temperatures in varying environmental conditions.[46] These advancements align with our approach of optimizing textile structures for enhanced thermal comfort, although our focus has been on different material combinations. Future work could explore integrating these electrospinning techniques with our TiO_2-GO composites to potentially further enhance the radiative cooling performance.

This study aims to manufacture, characterize, and evaluate a nanocomposite polymeric textile system incorporating GO nanosheets modified with titanium dioxide nanoparticles to improve thermal comfort through thermal energy dissipation by radiation and conduction. The process involves synthesizing and characterizing the nanoconjugate, followed by fabricating and evaluating the textile system, as illustrated in Figure 1.

2. MATERIALS AND METHODS

2.1. TiO_2-GO Nanoconjugates. *2.1.1. Synthesis.* GO was synthesized following the modified protocol developed at Universidad de los Andes.[47] In synthesis, 90 mL of 96% (v/v) sulfuric acid (PanReac AppliChem, Chicago, IL, USA) and 10 mL of 85% (v/v) phosphoric acid (J. T. Baker, Phillipsburg, NJ, USA) were mixed and slowly added to 0.75 g of graphite flakes (Graphene Supermarket, Ronkonkoma, NY, USA) and 4.5 g of potassium permanganate (PanReac AppliChem, Chicago, IL, USA). The resulting solution was allowed to react at 50 °C under constant magnetic stirring at 250 rpm for 12 h. To terminate the oxidation process, 150 mL of ice-cold Type I water was added, followed by the addition of 60 drops of 30% (w/w) hydrogen peroxide (PanReac AppliChem, Chicago, IL, USA), which induced a color change from dark purple to yellow. The resultant solution was then sonicated for 5 min at 38% amplitude and 40 kHz frequency, filtered with polyester fiber, centrifuged at 4000 rpm for 4 h at 4 °C, and resuspended in a washing solution composed of 37% (v/v) hydrochloric acid (PanReac AppliChem, Chicago, IL, USA), 96% ethanol (Ciacomeq, Bogotá DC. Colombia), and Type I water (1:1:1). This washing process was repeated three times. Subsequently, GO was washed twice with 96% ethanol and Type I water (1:1) and once with Type I water alone. The final GO pellet was lyophilized for 48 h and stored at 4 °C until further use.

TiO_2 NPs were silanized with (3-aminopropyl)-triethoxysilane (APTES). For this process, 100 mg of TiO_2 NPs (Sigma-Aldrich, St. Louis, MO, USA) were resuspended in 40 mL of Type I water. Then, 250 μL of 40% (v/v) tetramethylammonium hydroxide (TMAH) and 50 μL of glacial acetic acid (PanReac AppliChem, Chicago, IL, USA) were added to the solution, which was sonicated for 1 min at 38% amplitude and 40 kHz frequency and stirred for 3 min at 220 rpm. Subsequently, 1 mL of 20% (v/v) APTES solution (Sigma-Aldrich, St. Louis, MO, USA) was dripped under constant magnetic stirring at 220 rpm and 60 °C. The solution was then sonicated for 5 min under the same conditions, centrifuged at 4000 rpm for 4 h at 4 °C, and resuspended in Type I water. This process was repeated thrice, and the final TiO_2-APTES solution was lyophilized for 48 h and stored at 4 °C until further use.

GO was functionalized with polyethylene glycol (PEG) as follows: 14 mg of 1-ethyl-3-(3-(dimethylamino)propyl)-carbodiimide (EDC) and 7 mg of *N*-hydroxysuccinimide (NHS) (Sigma-Aldrich, St. Louis, MO, USA) were dissolved in 10 mL of Type I water under stirring for 10 min at 220 rpm and then added to 40 mL of GO at a concentration of 2.5 mg/mL. This reaction was carried out under constant magnetic stirring at 220 rpm for 15 min to activate the carboxyl-terminal groups of GO. Immediately afterward, 5 mL of H_2N−PEG600−NH_2 (Sigma-Aldrich, St. Louis, MO, USA) at a concentration of 0.5 mg/mL was added while stirring at 220 rpm for 24 h at 4 °C. The GO-PEG solution was then washed twice with Type I water and stored at 4 °C.

Finally, TiO_2-APTES NPs were conjugated with GO-PEG. A solution of APTES-TiO_2 in Type I water was prepared with 2 mL of 2% (v/v) glutaraldehyde (GA) (Sigma-Aldrich, St. Louis, MO, USA) and stirred for 1 h at 220 rpm. The TiO_2-APTES and GO-PEG solutions were then mixed and stirred together at 220 rpm for 24 h. Three formulations were prepared by varying the molar ratios of TiO_2 NPs to the free

https://doi.org/10.1021/acsomega.4c05600
ACS Omega 2024, 9, 49143−49162

carboxyl groups in the GO nanolayers: TiO_2-GO 1:1, TiO_2-GO 5:1, and TiO_2-GO 10:1. Each formulation underwent the same washing process as that previously described and was subsequently lyophilized for 48 h.

2.1.2. Physicochemical Characterization. The correct synthesis of GO, GO-PEG, TiO_2, TiO_2-APTES, TiO_2-GO 1:1, TiO_2-GO 5:1, and TiO_2-GO 10:1 was confirmed by Fourier transform infrared spectroscopy (FTIR) and thermogravimetric analysis (TGA). FTIR spectra were obtained using Alpha Eco-ATR equipment (Bruker, Germany) within the spectral range of 4000−500 cm^{-1}, with a resolution of 1 cm^{-1}. TGA was recorded on a SDT Q600 model (TA Instruments, New Castle, DE, USA). Samples weighing between 3 and 5 mg were analyzed over a temperature range of 25−600 °C at a heating rate of 10 °C/min under a N_2 atmosphere. The particle size distribution of TiO_2, TiO_2-APTES, TiO_2-APTES-GA, TiO_2-APTES-GA-PEG, and TiO_2-APTES-GA-PEG-GO was measured using a dynamic light scattering (DLS) instrument (Zeta-Sizer Nano-ZS, Malvern Instruments, Malvern, UK).

2.1.3. Morphological Analysis. The morphological and microstructural characteristics of GO, TiO_2, TiO_2-GO 1:1, TiO_2-GO 5:1, and TiO_2-GO 10:1 were analyzed using a scanning electron microscope model LYRA3 (TESCAN, Brno, Czech Republic) operated at an accelerating voltage of 10 kV. Energy dispersive X-ray spectroscopy (EDX) was employed to provide elemental composition information.

2.2. Textile Systems. *2.2.1. Manufacturing.* Recycled poly(ethylene terephthalate) (r-PET) from plastic bottles was used to prepare the textile systems. The r-PET was dissolved at a concentration of 15% (w/v) in ≥99% trifluoroacetic acid (TFA) (Sigma-Aldrich, St. Louis, MO, USA) at room temperature under constant magnetic stirring at 250 rpm for 24 h. Subsequently, one of three formulations of GO-TiO_2 at 1.5% (w/v) was added and left at room temperature under constant magnetic stirring at 250 rpm for an additional 2 h. The solution was then sonicated for 30 min at 38% amplitude and 40 kHz frequency.[48] Electrospinning was performed using an HZ-10 modular device (AME Energy, Linyi, China). A volume of 5 mL of the solution was deposited at a rate of 3 mL/h with a needle-to-collector distance of 12 cm and an applied voltage of 13 kV. The fibers were collected on a 3 cm diameter mandrel rotating at a speed of 100 rpm for 1 h. The resulting formulations were labeled as r-PET/TiO_2-GO $\boldsymbol{A/B}$, where $\boldsymbol{A/B}$ is the molar ratio of TiO_2 NPs to GO. The specific formulations produced were r-PET/TiO_2-GO 1:1, r-PET/TiO_2-GO 5:1, and r-PET/TiO_2-GO 10:1.

2.2.2. Physicochemical Characterization. The correct synthesis of r-PET, r-PET/GO, r-PET/TiO_2, r-PET/TiO_2-GO 1:1, r-PET/TiO_2-GO 1:5, and r-PET/TiO_2-GO 10:1 textiles was confirmed through TGA. Thermograms were recorded on a model SDT Q600 (TA Instruments, New Castle, DE, USA) with samples weighing between 3 and 5 mg, analyzed over a temperature range of 25−600 °C at a heating rate of 10 °C/min under N_2 atmosphere.

2.2.3. Morphological Analysis. Morphological and microstructural analyses of r-PET, r-PET/GO, r-PET/TiO_2, r-PET/TiO_2-GO 1:1, r-PET/TiO_2-GO 1:5, and r-PET/TiO_2-GO 10:1 textiles were analyzed using a SEM LYRA3 model (TESCAN, Brno, Czech Republic) operated at an accelerating voltage of 6 kV. Fiber diameters were estimated using ImageJ software. To ensure sample uniformity, fabric thicknesses were measured at ten distinct points within a 5 cm^2 area using a Mitutoyo 500-196-30 digital caliper (Kawasaki, Japan). This systematic approach was employed to verify the consistency of the samples following the manufacturing process.

2.2.4. Optical Analysis. The solar spectral reflectance of r-PET, r-PET/GO, r-PET/TiO_2, r-PET/TiO_2-GO 1:1, r-PET/TiO_2-GO 1:5, and r-PET/TiO_2-GO 10:1 textiles was measured by a Specord 50 Plus UV−vis spectrophotometer (Analytik Jena, Jena, Germany) equipped with a diffuse reflectance accessory with integrating sphere over the range of 400−1100 nm and a Nicolet iS50 FTIR spectrometer (Thermo Fisher Scientific, Waltham, MA, USA) with an integrating sphere over the range of 1100−2500 nm range. For the UV−vis range, a high diffuse reflectance white accessory was used as a control, while for the NIR range, the instrument's internal reference baseline was diffuse gold. The average reflectivity was calculated using the formula $\int_{0.4\mu m}^{2.5\mu m} I_{AM1.5}(\lambda) R(\lambda)\, d\lambda / \int_{0.4\mu m}^{2.5\mu m} I_{AM1.5}(\lambda)\, d\lambda$, where $R(\lambda)$ is the reflectance of the films from 0.4 to 2.5 μm and $I_{AM1.5}$ is the solar irradiance according to ASTM G173-23 standard. The transmittance/emittance of the samples was calculated using a previously calibrated FLIR E60 infrared camera (Teledyne FLIR, Wilsonville, OR, USA). Samples were placed on a heating plate at 35 °C, and the surface temperature was allowed to stabilize before infrared images were taken from a distance of 1 m. The percentage transmittance/emittance was then computed relative to the temperature values of the heating plate alone.

2.2.5. Thermal Conductivity. The thermal conductivity of r-PET, r-PET/GO, r-PET/TiO_2, r-PET/TiO_2-GO 1:1, r-PET/TiO_2-GO 1:5, and r-PET/TiO_2-GO 10:1 textiles was determined using a setup following the guidelines of the ISO 8302:1991 standard. Two LC-SSX1 heat exchanger devices (TE Technology, Traverse City, MI, USA) were each connected to two 0.2 mm diameter T-type thermocouples inserted through holes in the metal plates. One thermocouple was in direct contact with the plate, while the other was exposed to the environment at the plate's surface level. The thermocouples were secured with LOCTITE SI 5699 silicone (Henkel AG & Co. KGaA, Düsseldorf, Germany). The plates were thermally insulated using expanded polystyrene sheets, each connected to a PQ-12DC flow pump (Greylor Company, Cape Coral, FL, USA) and a W22 water bath (Anova Industries, New Providence, NJ, USA). The water baths were maintained at 25 and 34 °C to simulate ambient and skin temperatures, respectively, with pumps powered by a PSP-2010 power supply (GW Instek, New Taipei City, Taiwan) set at 7 V to circulate water through the systems. After 10 min of temperature stabilization, thermocouple data acquisition was initiated using an ADAM-4561-CE module (Advantech, New Taipei City, Taiwan) and LabVIEW visualization software (National Instruments, Austin, TX, USA). The temperature data stabilized over 10 min, after which a 5 cm square sample surrounded by a 0.2 mm thick expanded polystyrene sheet was placed to prevent heat transfer between the plates. Data were collected for 10 min and stored for later analysis. A time window of 5 s was chosen to calculate the thermal conductivity using the following equation: $k = Qd/A\Delta T$, where Q is the bath power (1200 W), d is fabric thickness (m), A is the cross-sectional area of the film (0.0016 m^2), and ΔT is the temperature differential (K).

2.2.6. Electro−Thermo−Mechanical Model of Microheater. Multiphysics simulations play a critical role during the early design stages of microsystems, enabling cost-effective optimization by modeling the complex interactions between

https://doi.org/10.1021/acsomega.4c05600
ACS Omega 2024, 9, 49143−49162

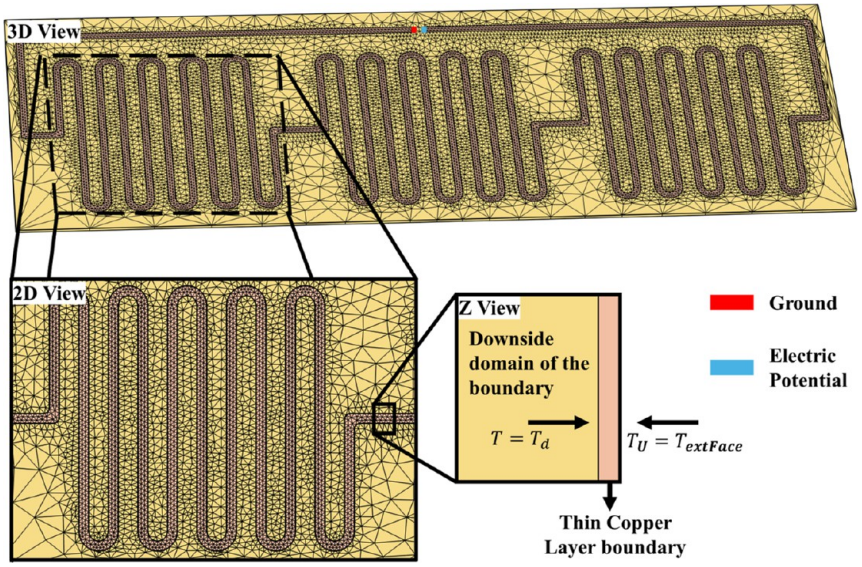

Figure 2. Mesh configuration and boundary conditions of microheater. Red is the ground, blue is the electric potential, yellow is the FR4 substrate, orange is the copper piste, *a* is the distance between piste, and *b* is the thickness of the copper piste. Scale bar: 1 cm.

the various phenomena occurring within these systems.[49−51] Additionally, they facilitate the identification of optimal operational conditions, ensuring that the systems function efficiently while significantly reducing development costs and enhancing design accuracy.[52] In this study, a comprehensive analysis was carried out using a thermo−electro−mechanical model within the COMSOL Multiphysics 6.2 (COMSOL Inc., Stockholm, Sweden) software to refine the geometry of planar resistors.[53] The primary objective of this simulation was to optimize the design of the resistors with particular emphasis on achieving a uniform temperature distribution. Such uniformity is essential for minimizing thermal fluctuations and reducing unwanted noise during outdoor testing. The thermal transport phenomena were governed by eq 1.

$$\rho C_p \frac{\partial T}{\partial t} + \nabla \cdot q = Q_{ted} + Q_I \tag{1}$$

where T is the absolute temperature within the system, ρ denotes the material density, C_p is the specific heat capacity, q is the heat flux, Q_I is the internal heat generation, resultant from the Joule heating effect, and Q_{ted} accounts for thermoelastic damping, as described by eq 2.

$$Q_{ted} = \alpha T : \frac{dS}{dt} \tag{2}$$

where α is the thermal expansion coefficient, and S is the second Piola−Kirchhoff stress tensor. To mitigate computational demand, the copper track was approximated as a thin layer, simplifying the model from three-dimensional to one-dimensional, as delineated by eq 3. This methodological condensation accelerates the computational process while preserving the core physical attributes of the system concentrating on the dominant directional phenomena.

$$\rho_{si} C_{p,si} \frac{\partial T_s}{\partial t} + \nabla_t \cdot q_{si} = Q_{si} \tag{3}$$

where T_s denotes an auxiliary dependent variable, residing within the product space, ρ_{si} is the layer density, $C_{p,si}$ is the heat capacity, Q_{si} characterizes the active heat source within the copper domain, and q is the conductive heat flux within the layer, which is further elaborated upon by eq 4.

$$q_{si} = -k_{si}(\nabla_t T_s + \nabla_n T_s) \tag{4}$$

where k_{si} is the thermal conductivity of the copper layer. Continuity between the comprehensive three-dimensional model and its one-dimensional simplification is achieved by enforcing boundary conditions, where $T = T_s$ is at the interface junctures. This pivotal linkage is numerically described by eqs 5 and 6 and is graphically shown in Figure 2.

$$T_d = (T_s)_{L=0} \tag{5}$$

$$T_u = (T_s)_{L=d} \tag{6}$$

where T_d represents the absolute temperature on the boundary's downside within the FR4 substrate, and T_u is the absolute temperature on the boundary's upper side, equivalent to the external environmental temperature.

Joule heating, often termed Ohmic or resistive heating, describes the conversion of electrical energy into thermal energy as an electrical current travels through a resistive medium. This phenomenon is quantitatively described in eq 7.

$$Q_I = J \cdot E \tag{7}$$

where J is the electric current density, as determined by eq 8, while E is the electric field, in accordance with eq 9.

$$J = \sigma \nabla V \tag{8}$$

$$E = -\nabla V \tag{9}$$

where σ is the electrical conductivity and V is the electrical potential. The deformation of the microheater was modeled utilizing a total Lagrangian formulation. This approach yielded the governing equation of motion (eq 10).

$$0 = \nabla \cdot S + F_V \tag{10}$$

where F_V is the volume force vector, and S is the second Piola−Kirchhoff stress. The thermal strain in the model is described in eq 11.

$$\varepsilon_{th} = \alpha(T - T_{ref}) \tag{11}$$

https://doi.org/10.1021/acsomega.4c05600
ACS Omega 2024, 9, 49143−49162

where α is the thermal expansion coefficient, which characterizes the material's deformation response to temperature changes relative to the reference temperature T_{ref}.

The subset of equations was solved using a stationary study utilizing the multifrontal massively parallel sparse direct solver (MUMPS), a solver optimized for efficiently handling large sparse linear systems through a multifrontal approach for both symmetric and unsymmetric matrices.[54,55] The employed mesh, detailed in Figure 2, was meticulously designed, featuring 96,611 domain elements, 193,289 boundary elements, and 10,757 nodes, ensuring mesh convergence. Parameters utilized in the models are comprehensively listed in Table 1.

Table 1. Simulation Parameters for the Electro−Thermo−Mechanical Model[a]

property	copper	FR4
thickness	35 [μm]	
heat capacity	100 [J/(kg K)]	250 [J/(kg K)]
thermal conductivity	100 [W/(m K)]	1.059 [W/(m K)]
electrical conductivity	5.96×10^7 [S/m]	
coefficient of thermal expansion	17×10^{-6} [1/K]	0.55×10^{-6} [1/K]

[a]References for the parameters used in the literature.[53]

2.2.6.1. Outdoor Measurements. For outdoor measurements, a custom device was designed to record temperature changes of simulated skin covered by different textiles under direct solar irradiance. A microheater simulated human skin was set at 35 °C using a current of 1.65 A at 1.3 V. A 0.2 mm diameter T-type thermocouple recorded the simulated skin temperature. The device walls and floor were made of expanded polystyrene insulation boards with four wooden pedestals attached to the bottom to mitigate thermal conduction effects. The insulation and wooden cubes were covered with aluminum foil to reflect sunlight and prevent heat ingress. A transparent sheet was placed on the roof to minimize the convective heat loss. The setup allowed the simultaneous measurement of six samples, eliminating the effect of the solar irradiance angle on textile cooling capabilities. Data acquisition followed the thermal conductivity guidelines.

2.2.6.2. Indoor Measurements. Indoor cooling properties were tested using the same setup as the outdoor tests with the thermocouples arranged to record the external textile temperature by placing the temperature sensors 1 cm above the samples and waiting for the system to stabilize.

2.2.7. Mechanical Properties. The mechanical properties of r-PET/GO, r-PET/TiO_2, r-PET/TiO_2-GO 1:1, r-PET/TiO_2-GO 1:5, and r-PET/TiO_2-GO 10:1 textiles were evaluated and compared with those of r-PET fabric. Stress−strain tests were performed using an 850 differential mechanical analysis machine (TA Instruments, New Castle, DE, USA) with a preload force of 5×10^{-3} N and a strain rate of 1 mm/min. Sample lengths and thicknesses were measured with a 500-196-30 digital caliper (Mitutoyo, Kawasaki, Japan) with a resolution of 0.01 mm.

2.2.8. Cell Viability. The viability of human skin keratinocyte cell line (HaCaT) on r-PET/GO, r-PET/TiO2,

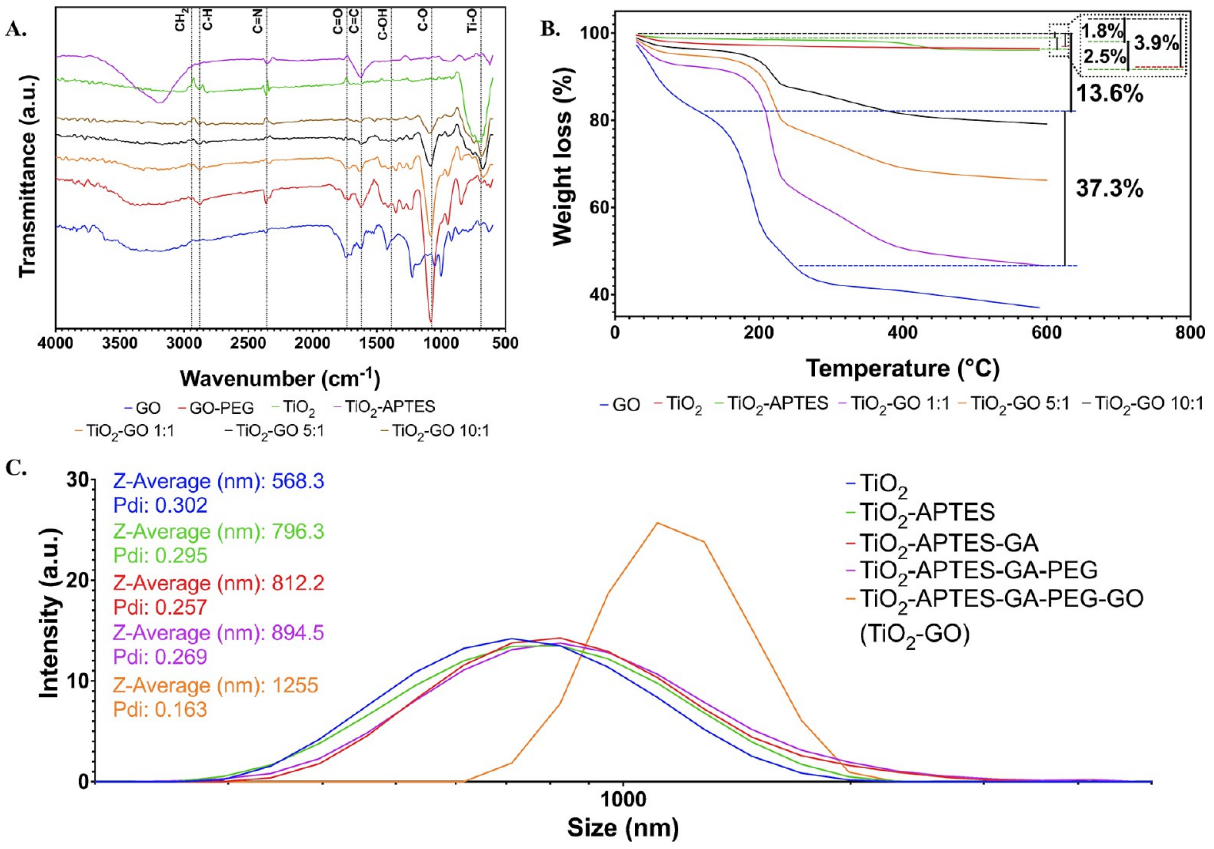

Figure 3. (A) FTIR spectra of TiO_2, TiO_2-APTES, GO, GO-PEG, TiO_2-GO 1:1, TiO_2-GO 5:1, and TiO_2-GO 10:1. (B) TGA thermograms of TiO_2, TiO_2-APTES, GO, TiO_2-GO 1:1, TiO_2-GO 5:1, and TiO_2-GO 10:1. (C) DLS histogram for the size intensity distribution of TiO_2-GO conjugate timeline.

https://doi.org/10.1021/acsomega.4c05600
ACS Omega 2024, 9, 49143−49162

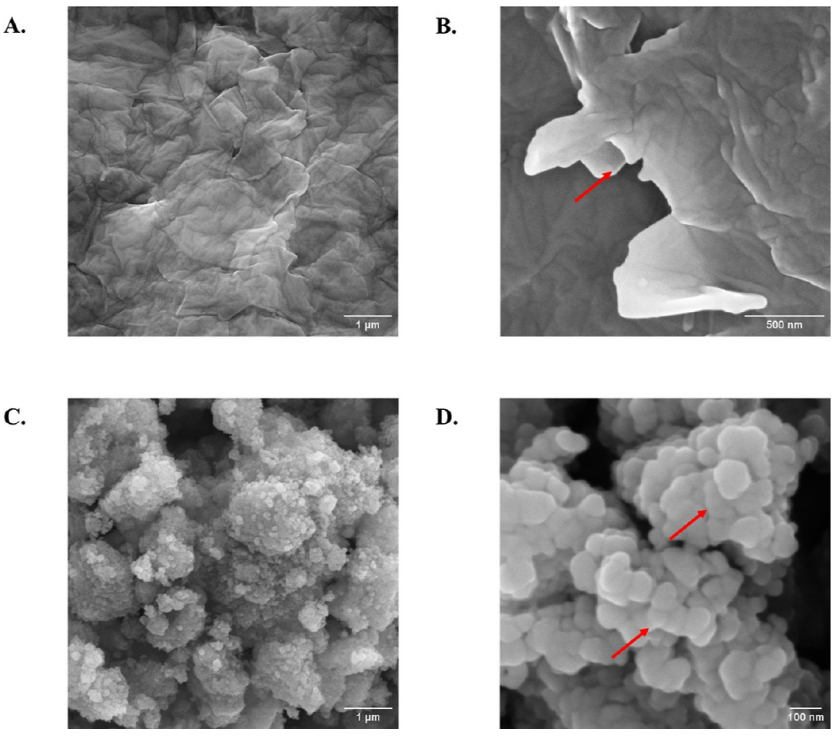

Figure 4. SEM images of GO (A,B) and TiO_2 (C,D) NPs at high (100 k×) and low magnification (30 k×) using an accelerating voltage of 10 kV. Red arrows in (B,D) indicate tightly stacked GO nanosheets and spherical aggregates of TiO_2 NPs, respectively.

r-PET, r-PET/GO, r-PET/TiO_2, r-PET/TiO_2-GO 1:1, r-PET/TiO_2-GO 1:5, and r-PET/TiO_2-GO 10:1 textiles was evaluated and compared to r-PET fabric using the 3-(4,5-dimethylthiazol-2-yl)-2,5-diphenyl tetrazolium bromide (MTT) assay. Samples of 25 mm^2 were cut from each formulation and sterilized in 96% ethanol for 12 h. Subsequently, the ethanol was removed, and the samples were immersed in Dulbecco's modified Eagle's medium (DMEM) (Biowest, Riverside, MO, USA) supplemented with 10% fetal bovine serum (FBS) and conditioned at 37 °C and 5% CO_2.

HaCaT cells were seeded in 96-well microplates with DMEM containing 10% FBS and 1% penicillin/streptomycin (P/S) at a concentration of 4×10^4 cells/mL. Cells were allowed to adhere for 24 h at 37 °C and 5% CO_2. Cells were then exposed to the different textile formulations for 24 and 72 h in a serum-free culture medium with 1% P/S. DMSO at 10% (v/v) concentration (PanReac AppliChem, Chicago, IL, USA) and untreated cells were used as negative and positive controls, respectively. After incubation, the textiles were removed, and MTT solution was added to each well to allow formazan crystals to form during an additional 2 h incubation. The medium was then removed, and DMSO was added to each well to dissolve the crystals. Absorbance was read at 595 nm.

2.2.9. Usability. To evaluate the wettability of the textile surfaces, contact angles were determined by measuring the tangent angle at the point of interfacial equilibrium using a 100 μL droplet of Type II water on a 1 cm^2 sample.

2.3. Statistical Analysis. Data analysis was carried out using GraphPad Prism 9.2.0 software (GraphPad Software, La Jolla, CA, USA). One-way ANOVA analyses with Tukey's multiple comparison test were used to examine statistical differences between the different textiles developed. Data were expressed as means with a standard deviation in the plots.

3. RESULTS AND DISCUSSION

3.1. TiO_2-GO Nanoconjugates. *3.1.1. Physicochemical Characterization.* The FTIR spectra of TiO_2, TiO_2-APTES, GO, GO-PEG, TiO_2-GO 1:1, TiO_2-GO 5:1, and TiO_2-GO 10:1 are presented in Figure 3A. The peak at 690.52 cm^{-1} corresponds to the stretching vibration of the Ti−O bond in the unfunctionalized nanoparticles.[56,57] Peaks at 1024 and 1120 cm^{-1} are associated with the stretching vibrations of the Ti−O−Si motif and the Si−O−Si bond, respectively, which result from the condensation reaction between the silanol groups of APTES and the hydroxyl groups on the TiO_2 surface.[58,59] The absorption band between 1500 and 1600 cm^{-1} is attributed to the scissor vibration of the NH_2 groups at the terminal end of the APTES molecules, while the small peak at 2940 cm^{-1} can be assigned to the CH_2 alkyl groups present in the same compound.[59] In APTES-TiO_2, a peak near 3200 cm^{-1} represents the stretching and bending vibrations of OH groups in atmospheric water molecules, on the nanoparticles, and the residual water remaining after freeze-drying.[57,60]

For GO, characteristic peaks are observed at 1734 cm^{-1} for C═O bond stretching vibration, at 1620 cm^{-1} for C═C aromatic bond bending vibration, at 1386 cm^{-1} for C−OH bond stretching vibration, and at 1073 cm^{-1} for C−O bond bending vibration.[61−63] The absence of a peak at 1250 cm^{-1} indicates a low reduction of GO.[64] In the PEG-GO spectrum, increases in peaks at 2878 cm^{-1} for the C−H bond stretching vibration and at 2231 cm^{-1} for the C═N bond stretching vibration are observed.[65,66] Upon GO-TiO_2 bonding, a shift of the Ti−O absorption band to lower wavelengths is observed, indicating the chemical interaction between the surface hydroxyl groups of TiO_2 and the functional groups of GO.[67]

The thermal stability of TiO_2, TiO_2-APTES, GO, TiO_2-GO 1:1, TiO_2-GO 5:1, and TiO_2-GO 10:1 was evaluated using TGA, as shown in Figure 3B. The thermogram shows a weight

https://doi.org/10.1021/acsomega.4c05600
ACS Omega 2024, 9, 49143−49162

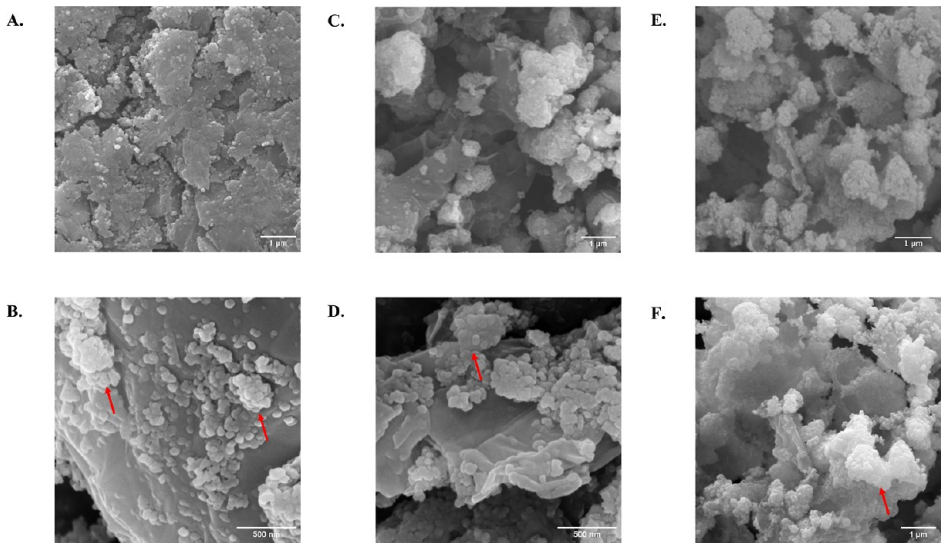

Figure 5. SEM images of TiO_2-GO 1:1 (A,B), TiO_2-GO 5:1(C,D), and TiO_2-GO 10:1 (E,F) nanoconjugates at high (100 k×) and low magnification (30 k×) utilizing an accelerating voltage of 10 kV. The red arrows in (B) indicate nonuniformly dispersed TiO_2 NPs on the GO nanolayer, while those in (D) show a better distribution of TiO_2 NPs on the surface of the nanolayer. The red arrow in (F) highlights a large cluster of TiO_2 NPs, which obscure the GO structure.

loss of 3.9% for TiO_2, which is associated with the evaporation of water on the surface of the nanoparticles.[68] For TiO_2-APTES, a weight loss of 1.8% is observed at temperatures below 200 °C. A second weight loss of 2.5% from 200 to 800 °C is due to thermal decomposition of the silane agent.[68] The GO thermogram shows a 13.6% weight loss from 30 to 100 °C, associated with water evaporation, and a second weight loss of 37.3% between 100 and 250 °C, attributed to the removal of oxygenated species such as C−O, C−OH, and C═O in the GO.[64] As the molar ratio of TiO_2-GO increase, the thermal stability of the nanoconjugates also increases.[69] The reduced amount of free oxygenated groups on the GO surface decreases as the ratio of TiO_2 NPs rises, resulting in a smaller weight loss in the second region of the TiO_2-GO 10:1 thermogram compared to TiO_2-GO 1:1 and TiO_2-GO 5:1.

To confirm the TiO_2-GO binding, an additional DLS analysis was performed to corroborate that each individual step of the process generated a larger nanoconjugate diameter (Figure 3C). The TiO_2 NPs exhibit an average hydrodynamic diameter (*Z*-average) of 568.3 nm with a polydispersity index (PdI) of 0.302. Comparisons with captured SEM images show that the DLS technique presents five times larger sizes.[70] Upon conjugation of the nanoparticles with APTES, an increase in the *Z*-average to 796 nm with a PdI of 0.295 demonstrates the correct incorporation of the linker by the TiO_2 NPs. Similarly, the binding of the GA cross-linker to TiO_2-APTES indicated *Z*-average values of 812.2 nm with a PdI of 0.257, and the subsequent attachment of the PEG linker generated an increase of 82.3 nm (*Z*-average: 894.5 nm; PdI: 0.269). The final GO conjugation in the system resulted in the largest size increase to a *Z*-average of 1255 nm and a PdI of 0.163, reflecting the size difference between nanolayers and nanoparticles.

3.1.2. Morphological Analysis. Figures 4 and 5 illustrate the surface morphology of GO, TiO_2, TiO_2-GO 1:1, TiO_2-GO 5:1, and TiO_2-GO 10:1 as observed using SEM. Figure 4A,B reveals the characteristic wrinkled and fluffy structure of GO, showing a disordered arrangement of the nanolayers.[71] Figure 4C,D shows the typical spherical shape of the TiO_2 nanoparticles with diameters of approximately 100 nm and the formation of nonuniform aggregates in size.[72] In the nanoconjugates shown in Figure 5, TiO_2 NPs are attached to the GO surface, demonstrating successful conjugation.[73] In the TiO_2-GO 1:1 molar ratio, partial dispersion of the nanoparticles within the nanosheets is observed, whereas in the TiO_2-GO 10:1 molar ratio, aggregates tend to form due to the higher nanoparticle concentrations used[74] (Figure 5A,B,E,F). A more uniform distribution of the TiO_2 NPs within the GO is observed at the TiO_2-GO 5:1 molar ratio (Figure 5C,D).

The compositional analysis by EDX is summarized in Table 2. The EDX spectrum of GO indicates that the main elements

Table 2. EDX Analysis Results for GO Nanolayers, TiO_2 NPs, TiO_2-GO 1:1, TiO_2-GO 5:1, and TiO_2-GO 10:1 Nanoconjugates

element	GO	TiO_2	TiO_2-GO 1:1	TiO_2-GO 5:1	TiO_2-GO 10:1
carbon (%)	58.73	11.25	56.96	27.18	23.05
oxygen (%)	36.53	48.29	29.36	38.72	43.87
titanium (%)		40.05	13.69	34.10	33.08
sulfur (%)	4.23	0.41			
chlorine (%)	0.51				

in the nanolayers are carbon and oxygen, with weight percentages of 58.73% and 36.53%, respectively.[75] This confirms the successful oxidation process due to the significant number of oxygenated groups on the GO surface. The presence of sulfur and chlorine in the nanoconjugate results from residues left over from the washing process. EDX analysis of TiO_2 NPs shows the presence of oxygen, titanium, and carbon elements.[76] The detection of carbon, oxygen, and titanium in the TiO_2-GO nanoconjugates confirms the conjugation of TiO_2 NPs to GO.[77] As the molar ratio of TiO_2 to GO increases, the amount of detected carbon decreases due to lower exposure of the nanolayers, while the proportion of oxygen increases and titanium decreases because TiO_2 NPs have a 2:1 ratio of oxygen to titanium. Similar

https://doi.org/10.1021/acsomega.4c05600
ACS Omega 2024, 9, 49143−49162

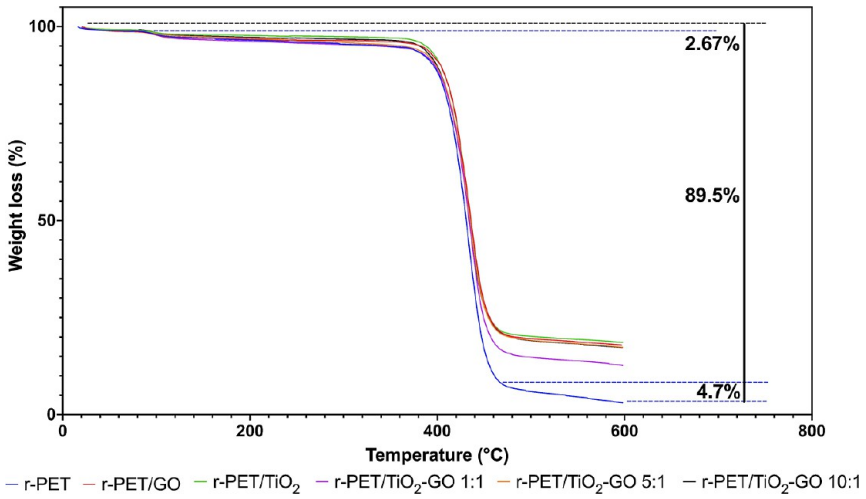

Figure 6. FTIR spectra of electrospun r-PET, r-PET/GO, r-PET/TiO_2, r-PET/TiO_2-GO 1:1, r-PET/TiO_2-GO 5:1, and r-PET/TiO_2-GO 10:1 textiles.

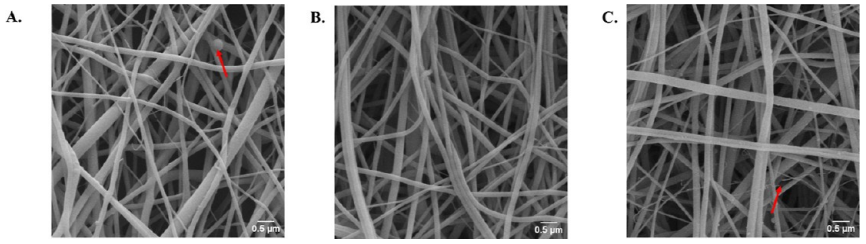

Figure 7. SEM images of r-PET nanofibers electrospun from a solution of (A) 10, (B) 15, and (C) 20% (w/v) concentration at 30 k× magnification and 6 kV accelerating voltage. The red arrow in (A) indicates agglomerates of the polymer within the nanofiber structure, while the red arrow in (C) highlights the breakage of the r-PET fibers due to the insufficient formation of the polymer chain network.

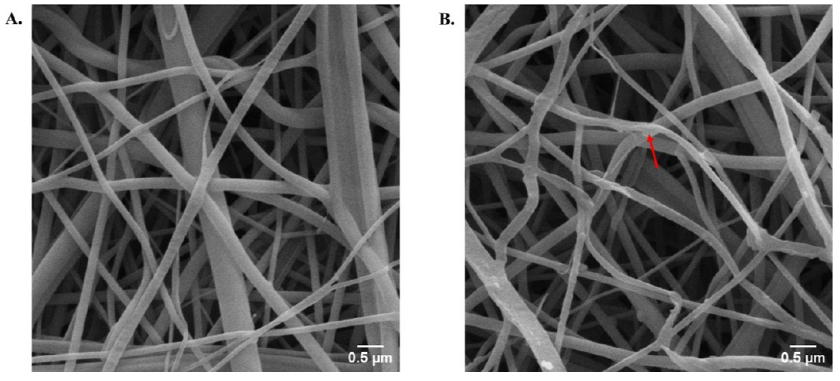

Figure 8. SEM images of r-PET nanofibers filled with (A) 1.5, and (B) 3 wt % TiO_2-GO concentration at 30 k× magnification and 6 kV accelerating voltage. The red arrow in (B) indicates a node-like lump and irregular morphology in the r-PET fiber resulting from the use of a high concentration of the TiO_2 NPs with GO nanoconjugate.

percentages are observed in studies where TiO_2 NPs are conjugated to GO at low molar ratios.[78]

3.2. Textile Systems. *3.2.1. Physicochemical Characterization.* Figure 6 shows the thermograms of rPET, rPET/GO, rPET/TiO_2-GO 1:1, rPET/TiO_2-GO 5:1, and rPET/TiO_2-GO 10:1 textiles. The thermogram of r-PET shows an initial weight loss close to 3% between 90 and 100 °C, associated with the evaporation of water molecules from the fiber surface. A second significant weight loss of 89.62% occurs up to 470 °C because of the decomposition of the r-PET backbone.[79] A third weight loss of approximately 5% up to 600 °C results from the decomposition of residual material from the second loss.[80] The remaining residue is 3.05%. The incorporation of compounds into r-PET reduces the movement of molecular chains, decreasing the crystallization rate and enhancing the thermal stability to the textile.[81] The inorganic nature of the nanoparticles results in low degradability at high temperatures, increasing the char amount to 18.64%.[82] GO also presents high thermal stability, providing a residual mass of 17.93%[83] when incorporated into the textile. Consequently, as the percentage of TiO_2 NPs decreases with the molar ratio, the thermal stability also decreases from 17.31% to 12.1%.

3.2.2. Morphological Analysis. A preliminary study was developed to determine the optimal electrospinning conditions for r-PET used in this study. Figure 7 shows the SEM image of the r-PET nanofibers developed at 10%, 15%, and 20% (w/v)

https://doi.org/10.1021/acsomega.4c05600
ACS Omega 2024, 9, 49143−49162

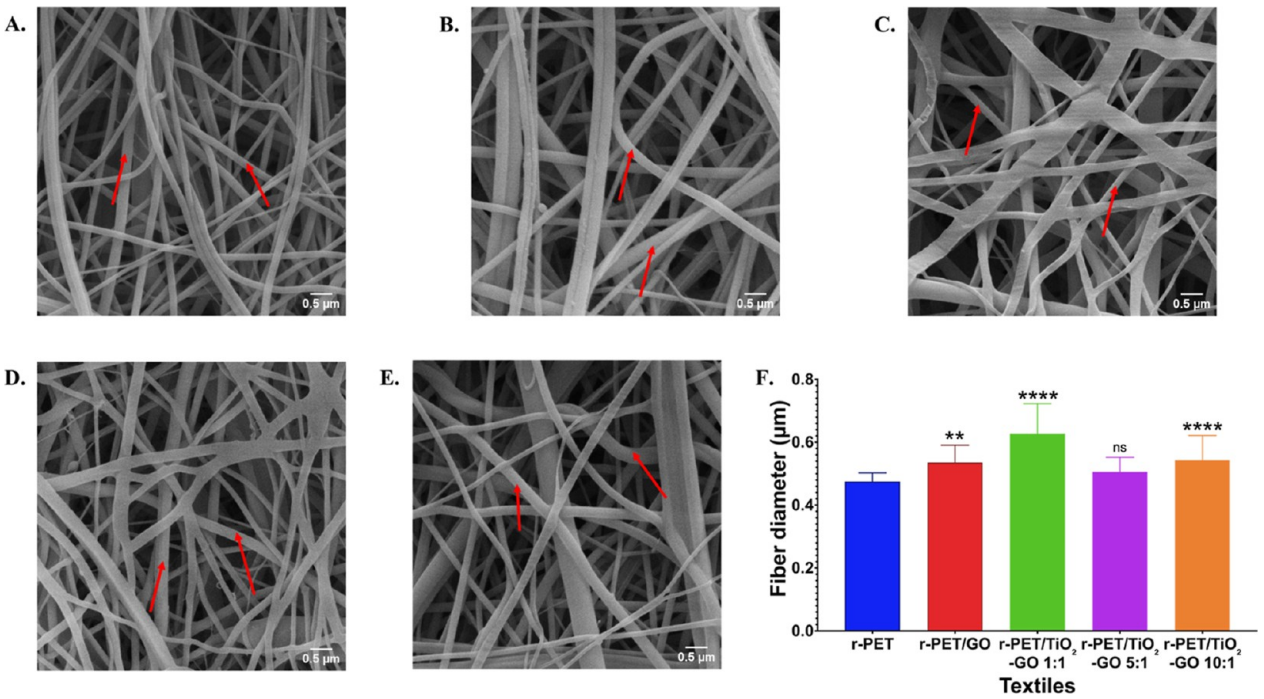

Figure 9. SEM images of (A) rPET, (B) rPET/GO, (C) rPET/TiO_2-GO 1:1, (D) rPET/TiO_2-GO 5:1, and (E) rPET/TiO_2-GO 10:1 at 30 k× magnification and 6 kV accelerating voltage and (F) diameter distribution of textile fibers. The red arrows indicate defect-free fibers in the developed formulations, attributed to optimal electrospinning parameters.

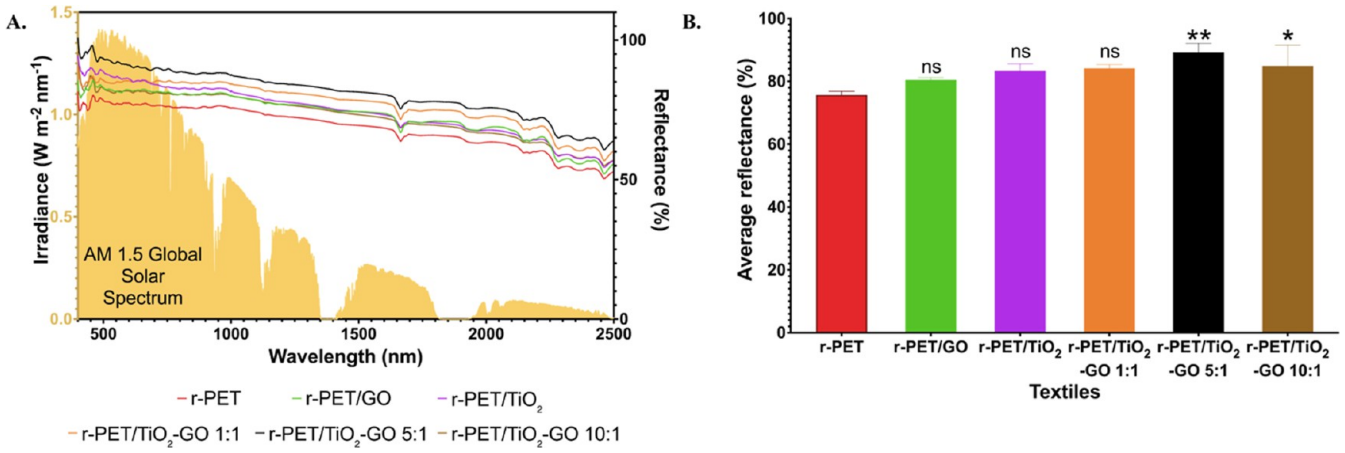

Figure 10. Reflectivity (A) spectrum and (B) values of r-PET, r-PET/GO, r-PET/TiO_2, r-PET/TiO_2-GO 1:1, r-PET/TiO_2-GO 5:1, and r-PET/TiO_2-GO 10:1 textiles in the 0.4−2.5 μm wavelength range.

in TFA. As evidenced in Figure 7A, a 10% (w/v) concentration of r-PET produces fibers with defects due to insufficient interlacing of the polymer chains.[84] Increasing the concentration to 15% (w/v) yields defect-free fibers with homogeneous sizes, as shown in Figure 7B. At this concentration, the polymer solution forms a network of r-PET chains that prevent fiber breakage during electrospinning.[85] When the r-PET concentration is increased to 20% (w/v), fibers adhere to each other with varying sizes (Figure 7C). Therefore, an r-PET concentration of 15% (w/v) was chosen for further experiments.

The morphology of r-PET fabrics loaded with TiO_2-GO is shown in Figure 8. At a nanocomposite concentration of 1.5% (w/w) relative to the polymer, fibers with uniform and smooth surfaces are observed (Figure 8A). Increasing the nanocomposite concentration to 3% (w/w) generates fibers with irregular and lumpy morphologies (Figure 8B) due to the agglomeration of GO during the electrospinning process caused by a phase separation with the polymer solution.[86] Thus, a nanoconjugate concentration of 1.5% (w/w) was chosen.

Figure 9 shows the morphology of r-PET fabrics at a concentration of 15% (w/v) with nanoconjugates at a concentration of 1.5% (w/w) and varying molar ratios between GO and TiO_2. The r-PET and r-PET/GO fabrics are also presented for comparison. As shown in Figure 9A, the average diameter of r-PET fibers is 0.48 μm, which agrees well with previous studies.[87] When GO is added at concentrations higher than 1% (w/w) relative to r-PET (as in the r-PET/GO textile), the fiber diameter increases to 0.54 μm because of the nonhomogeneity and agglomeration of the nanolayers in the electrospinning solution[83] (Figure 9B). As the molar ratio

https://doi.org/10.1021/acsomega.4c05600
ACS Omega 2024, 9, 49143−49162

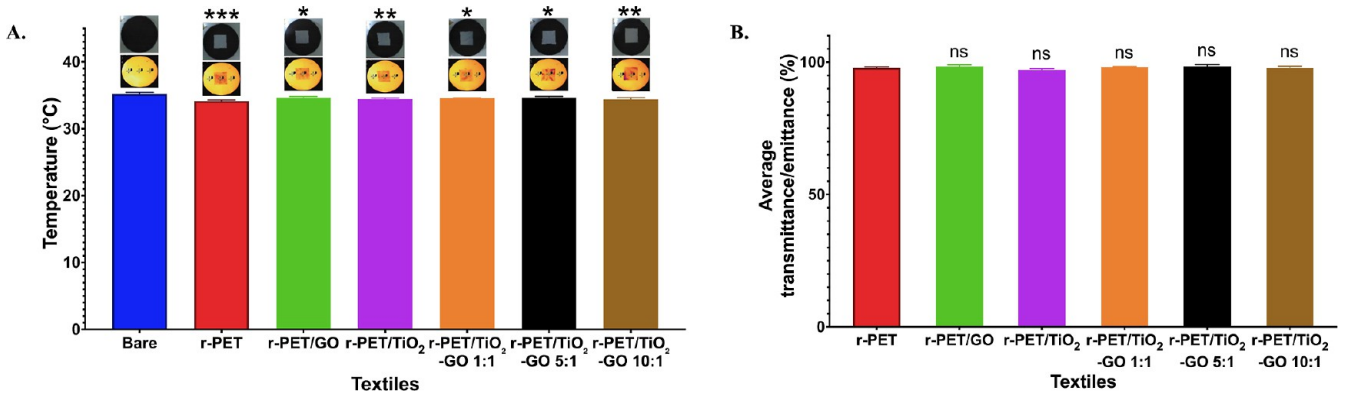

Figure 11. (A) Surface temperature (including corresponding infrared and digital images of samples for comparison) and (B) transmissivity/emissivity values of r-PET, r-PET/GO, r-PET/TiO_2, r-PET/TiO_2-GO 1:1, r-PET/TiO_2-GO 5:1, and r-PET/TiO_2-GO 10:1 textiles.

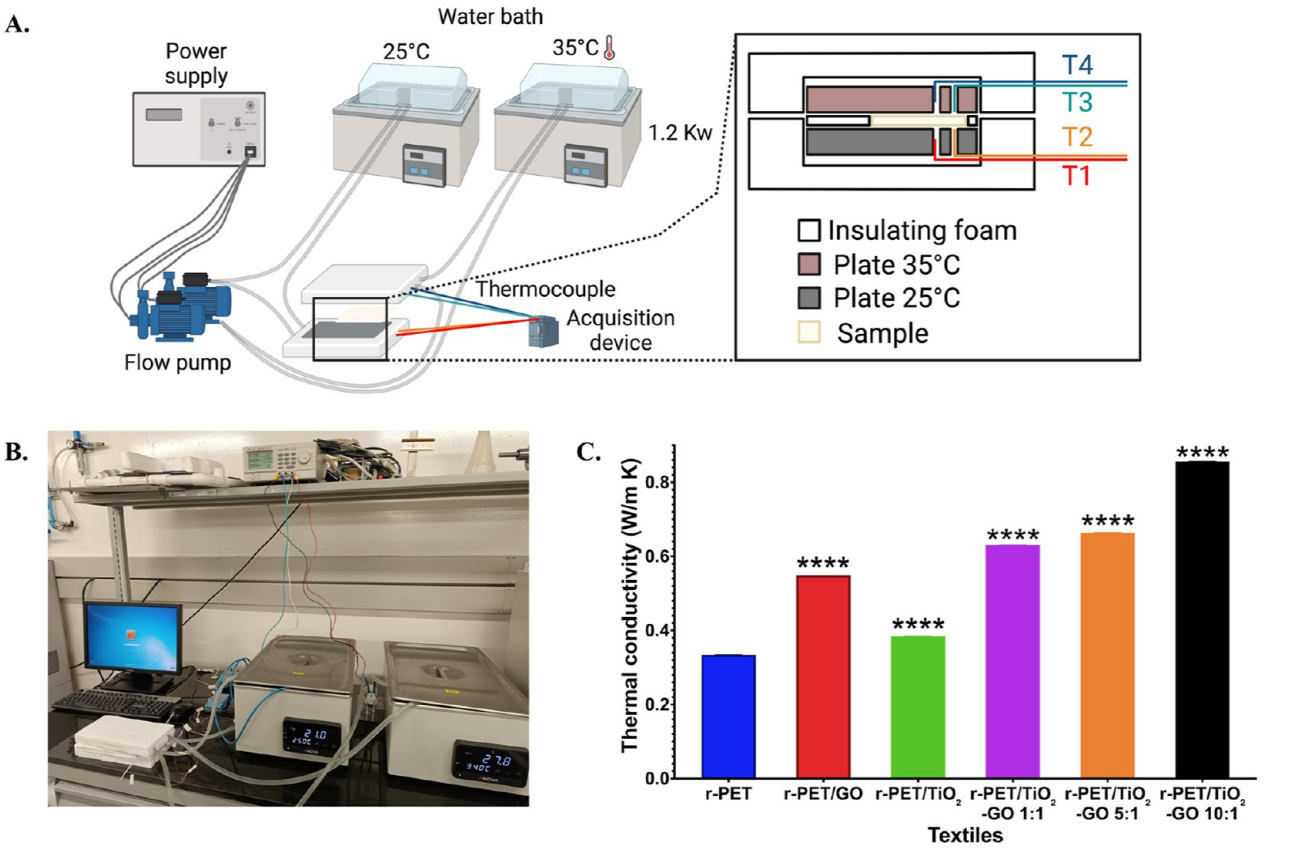

Figure 12. Thermal conductivity (A) schematic of the setup, (B) picture of the homemade assembly, and (C) coefficients of r-PET, r-PET/GO, r-PET/TiO_2, r-PET/TiO_2-GO 1:1, r-PET/TiO_2-GO 5:1, and r-PET/TiO_2-GO 10:1 textiles.

between the nanoconjugate elements increases, the fiber size increases for r-PET/TiO_2-GO 5:1 and r-PET/TiO_2-GO 10:1 textiles, reaching values of 0.51 and 0.54 μm (Figure 9D,E). This happens because the fiber diameter and GO ratio have an inverse relationship, while the fiber size and TiO_2 NPs concentration have a direct relationship at low weight concentrations of both components. As the GO concentration decreases, the electrical conductivity of the solution decreases, leading to an increase in fiber size.[88] Conversely, as the TiO_2 NPs concentration increases, the viscosity and surface tension of the electrospinning solution rise, increasing the fiber diameter in the fabric.[89] The r-PET/TiO_2-GO 1:1 textile exhibits a slightly different behavior with fiber diameter values of 0.63 μm (Figure 9C). The fiber diameter distribution is shown in Figure 9F. The electrospinning parameters were standardized to produce textiles with consistent thickness across the areas used for various measurements. As a result, the textiles exhibited a mean thickness of 131.00 ± 5.68 μm, corresponding to a deviation of only 4.33% within the measured area, indicating a high degree of uniformity.

3.2.3. Optical Analysis. The spectral solar reflectance of the developed textiles is shown in Figure 10A. In all cases, higher reflectance percentages are observed in the vis spectrum (300−800 nm), which correlates with the fiber diameter distribution shown in Figure 9F. According to the Mie theory, fiber diameters have a direct relationship with light scattering.[90] The reflectance values for r-PET, r-PET/GO, r-PET/TiO_2, r-PET/TiO_2-GO 1:1, r-PET/TiO_2-GO 1:5, and r-PET/TiO_2-GO

https://doi.org/10.1021/acsomega.4c05600
ACS Omega 2024, 9, 49143−49162

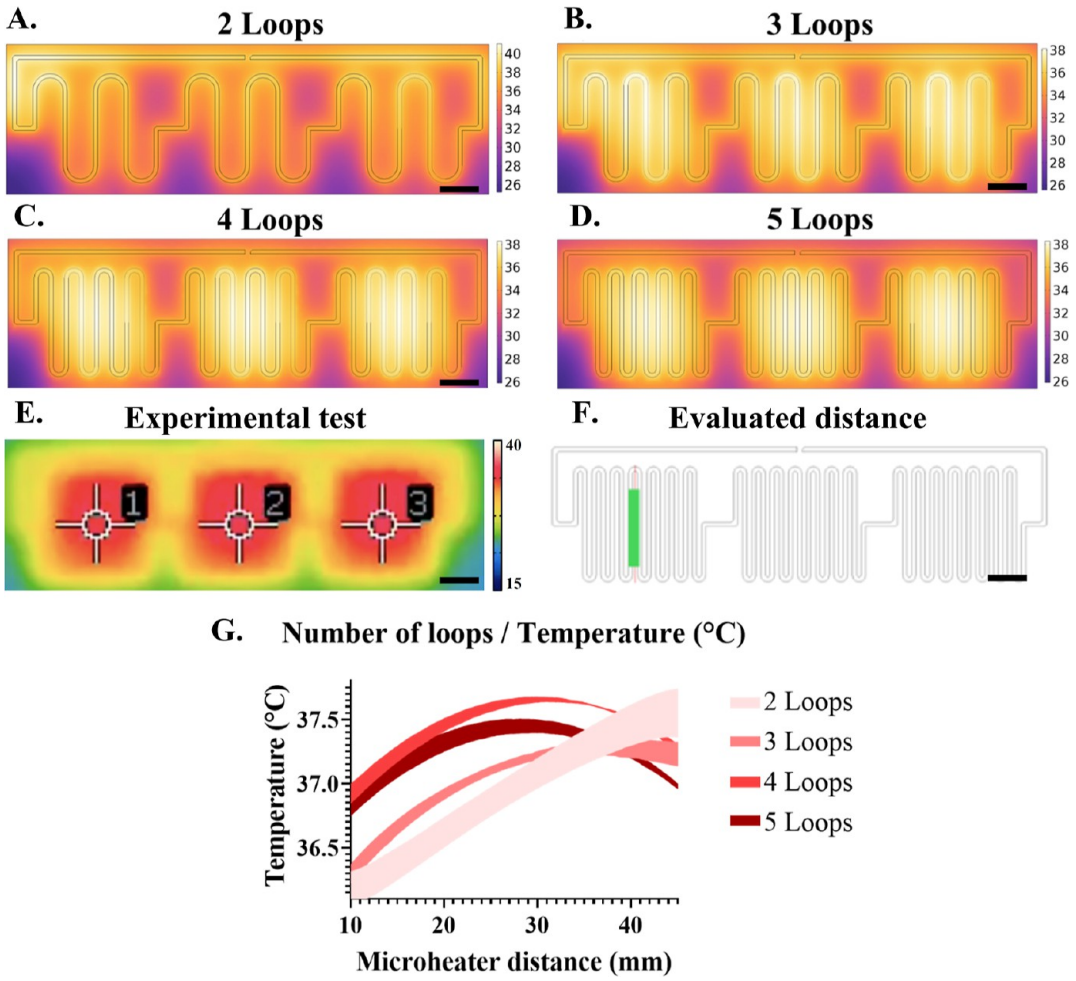

Figure 13. Electro−thermo−mechanical simulation results for microheaters with varying loop configurations, alongside the experimental temperature map. (A−D) Simulated thermal maps for microheaters with 2, 3, 4, and 5 loops, respectively. (E) Experimental heat map of the manufactured microheater with 5 loops. (F) Measurement distance of the temperature profile evaluated in panel (G). (G) Line graph of temperature variation as a function of distance across the microheater. Scale bar: 2 cm.

10:1 textiles are 75.64%, 80.45%, 83.36%, 84.08%, 89.26%, and 84.88%, respectively, as illustrated in Figure 10B. The r-PET textiles exhibit the lowest reflectivity values, while the r-PET/TiO_2-GO 5:1 formulation shows the highest reflectance, with a nearly 10% difference between the two groups. A decrease in reflectivity is observed when increasing the molar ratio of TiO_2 to GO to 10:1, the nanoparticles in the initial electrospinning solution,[18] as shown in Figure 8. This effect is more pronounced in the r-PET/TiO_2 formulation, which correlates with its lower thermal performance. It has been shown that the refractive index of TiO_2 NPs can vary depending on aggregate size.[91] In the case of GO, a slight increase in reflectivity compared to r-PET is observed, possibly due to the orientation of some sheets within the fiber when it interacts with the light beam.

Infrared images and surface temperatures of the textiles are presented in Figure 11A. Textiles with low statistical differences relative to the control are the r-PET/TiO_2-GO 1:1, r-PET/TiO_2-GO 1:5, and r-PET-GO formulations, with temperature differences of 0.57−0.63 °C. This is a result of a lower amount of material that can interfere with wavelengths in the infrared spectrum.[19] Additionally, GO can increase the transmittance/emittance of films in this range through the characteristic vibrational transitions of its main groups.[92,93] Incorporating large amounts of nanoparticles generates wavelength scattering within the film, reducing transmittance and emittance in the infrared spectrum. This phenomenon supports the results for r-PET/TiO_2 and r-PET/TiO_2-GO 1:10 textiles, where particle agglomeration occurs on the nanolayers, as shown in Figure 4C−F. However, it is important to emphasize that the r-PET textile shows an average surface temperature of 34.17, 1.03 °C lower than the control, demonstrating the significance of incorporating polymers with low absorption peaks at wavelengths between 7 and 13 μm.[94,95] This behavior is validated by Figure 11B, where transmittance/emittance percentages are 97.07%, 98.40%, 97.82%, 98.20%, 98.40%, and 97.73% for r-PET, r-PET/GO, r-PET/TiO_2, r-PET/TiO_2-GO 1:1, r-PET/TiO_2-GO 5:1, and r-PET/TiO_2-GO 10:1 textiles, respectively.

3.2.4. Thermal Conductivity. The thermal conductivity results of the textiles are shown in Figure 12. Using the setup shown in Figure 12A,B, it is established that the r-PET textile exhibits the lowest thermal conductivity, with values close to 0.35 W/m K. This demonstrates that polymers used in textile materials typically have low thermal performance due to their disordered structure.[96] Polyethylene films manufactured using the electrospinning technique at acceleration voltages of 13 kV also show thermal conductivity values lower than 1 W/m K.[97]

https://doi.org/10.1021/acsomega.4c05600
ACS Omega 2024, 9, 49143−49162

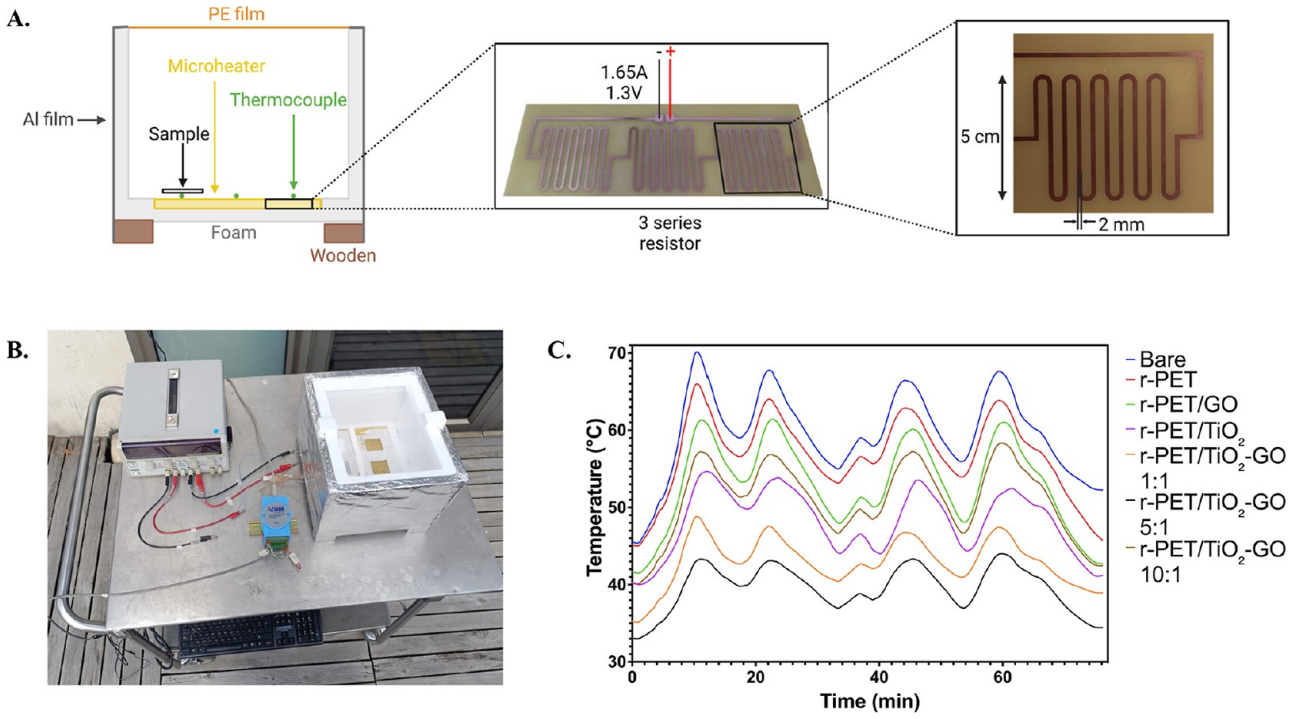

Figure 14. Measuring the thermal cooling performance of textiles outdoors. (A) Schematic of the setup used to measure the temperature of the simulated skin covered with the fabrics. (B) Photograph of the experimental setup under direct solar irradiance. The setup features a microheater designed to replicate the thermal properties of human skin. The microheater is connected to a power source to maintain a stable temperature of 35 °C using a current of 1.65 A, ensuring consistent conditions throughout the experiment. A 0.2 mm diameter T-type thermocouple is attached directly to the microheater to record real-time temperature data. The device is enclosed with walls and a floor made of expanded polystyrene insulation boards supported by four wooden pedestals at the bottom to reduce thermal conduction, all covered in aluminum foil to reflect sunlight. A transparent polymer cover reduces convective heat loss. (C) Temperature data of the microheaters with the textiles on their surface under sunlight for 70 min in Bogota.

Incorporating GO into the fibers results in a significant increase of almost 65% in thermal conductivity, reaching 0.55 W/m K. This improvement is due to the low interfacial thermal resistance between GO and the polymer.[84] The r-PET/TiO_2 textile also presents enhanced thermal conductivity compared to r-PET, with values reaching 0.38 W/m K. This behavior can be attributed to increased thermal transfer facilitated by interactions among the nanoparticles.[98] Increasing the molar ratio between TiO_2 NPs and GO further enhances thermal conductivity, with values rising from 0.63 to 0.85 W/m K. GO nanosheets act as a support structure, distributing the TiO_2 NPs and enhancing interactions between the components of the nanoconjugates.[99] As the molar ratio of the nanoconjugate increases, kinks in the nanolayers that can lead to inhomogeneous heat transfer are avoided. This results in a larger surface area for dissipating thermal energy due to the increased amount of conjugated nanoparticles (Figure 12C).

3.2.5. Textile System Thermal Measurements. 3.2.5.1. Outdoor. The cooling performance of the textiles was examined when placed in the homemade assembly under sunlight in Bogota (Figure 14A). The microheater was connected to a power supply at a constant current to achieve a temperature of 35 °C and was inserted in an expanded polystyrene box with wooden bases and covered with a transparent film to avoid thermal conduction and convection, respectively. A thermocouple was placed under the textile to understand its effect on the surface temperature of the simulated skin (Figure 14B). When covered with the r-PET, r-PET/GO, r-PET/TiO_2, r-PET/TiO_2-GO 1:1, r-PET/TiO_2-GO 5:1, y r-PET/TiO_2-GO 10:1, the skin temperature was 2.80, 6.62, 11.40, 16.64, 20.06 and 8.63 °C lower, respectively, than when no fabric was placed over the resistor (Figure 14C). This information evidences that the r-PET textile can help reflect sunlight in outdoor environments, as it shows a difference of almost 3 °C in the average temperature recorded by the simulated skin. The r-PET/TiO_2-GO 5:1 formulation presents the smallest temperature difference, as suggested by the reflectance data in the UV-−vis−-NIR spectrum. The orderly arrangement without large agglomerates of TiO_2 NPs on GO, good thermal conductivity, and the size of the fibers in the relevant wavelength range contribute to its superior outdoor cooling properties. The r-PET/TiO_2-GO 1:1 textile ranks second due to the lack of nanoparticles on the surface of the nanolayers, which limits the average reflectivity of the films. Smaller temperature differences are observed for the r-PET/TiO_2 and r-PET/TiO_2-GO 10:1 textiles due to agglomerates formed in the formulations. GO does not significantly affect reflectivity in the solar spectrum.

3.2.5.2. Optimization of Microheater Designs. Electro−thermo−mechanical simulations of microheaters with varying loop configurations provided valuable insights into optimizing temperature distribution. As illustrated in Figure 13A−D, the designs ranged from two to five loops. Notably, increasing the number of loops was directly associated with enhanced thermal uniformity. The two-loop configuration displayed the most uneven temperature distribution, with significant variations across the microheater surface, making it unsuitable for applications requiring consistent heating. In contrast, the

https://doi.org/10.1021/acsomega.4c05600
ACS Omega 2024, 9, 49143−49162

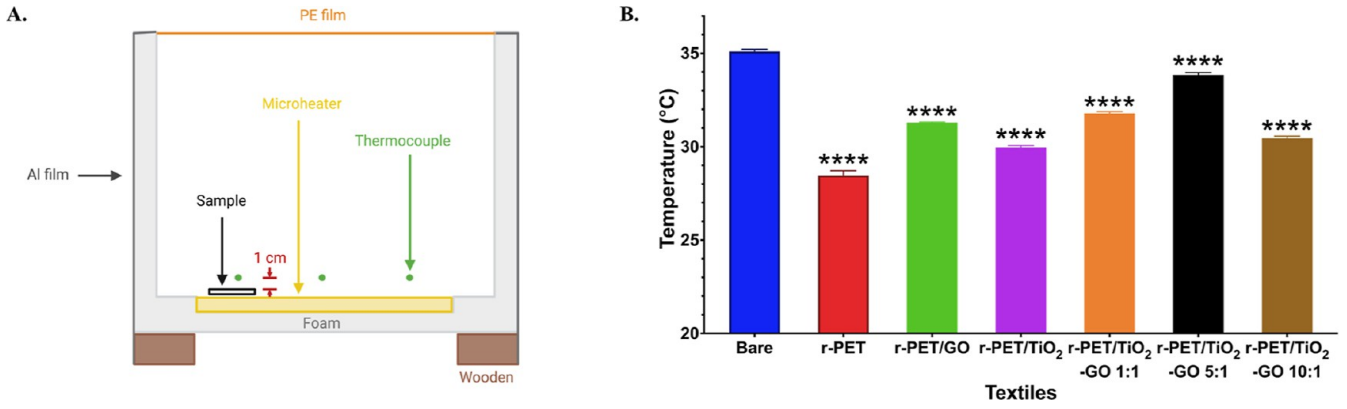

Figure 15. (A) Schematic of the indoor measuring device. (B) Temperature of the external surface of the textiles on the simulated skin.

five-loop configuration exhibited exceptional thermal uniformity with minimal variation (approximately 0.5 °C).

Based on the superior performance demonstrated in the simulations, the five-loop configuration was selected for manufacturing. The experimental results, presented in Figure 13E, validate the findings of the simulations and confirm that this configuration provides the most uniform temperature distribution.

Further analysis revealed that microheaters with three to five loops not only achieved improved thermal uniformity but also exhibited reduced resistance deviation during simulations. This suggests that these configurations enhance the electrical stability, a crucial factor for the operational reliability of microheaters. Figure 13F,G further illustrates these findings. Figure 13F shows the evaluation line used to measure the temperature across the microheater, while Figure 13G plots the temperature values along this line, confirming the minimal variation achieved with the five-loop design.

This five-loop design, optimized for uniform temperature distribution and enhanced electrical stability, is ideally suited for experimental tests simulating the human body temperature.

The cooling performance of the textiles was examined when placed in a homemade assembly under sunlight in Bogota (Figure 14A). The microheater was connected to a power supply at a constant current to achieve a temperature of 35 °C and was inserted in an expanded polystyrene box with wooden bases and covered with a transparent film to avoid thermal conduction and convection, respectively. A thermocouple was placed under the textile to understand its effect on the surface temperature of the simulated skin (Figure 14B). When covered with the r-PET, r-PET/GO, r-PET/TiO_2, r-PET/TiO_2-GO 1:1, r-PET/TiO_2-GO 5:1, and r-PET/TiO_2-GO 10:1 textiles, the skin temperature was 2.80, 6.62, 11.40, 16.64, 20.06, and 8.63 °C lower, respectively, than when no fabric was placed over the resistor (Figure 14C). This information evidences that the r-PET textile can help reflect sunlight in outdoor environments, as it shows a difference of almost 3 °C in the average temperature recorded by the simulated skin. The r-PET/TiO_2-GO 5:1 formulation presents the smallest temperature difference, as suggested by the reflectance data in the UV−vis−NIR spectrum. The orderly arrangement without large agglomerates of TiO_2 NPs on GO, good thermal conductivity, and the size of the fibers in the relevant wavelength range contribute to its superior outdoor cooling properties. The 1:1 r-PET/TiO_2-GO textile ranks second due to the lack of nanoparticles on the surface of the nanolayers, which limits the average reflectivity of the films. Smaller temperature differences are observed for the r-PET/TiO_2 and r-PET/TiO_2-GO 10:1 textiles due to agglomerates formed in the formulations. GO does not significantly affect the reflectivity in the SS.

3.2.5.3. Indoor. The indoor thermal properties of the textiles were measured using the assembly with the microheaters, the thermocouples, a thermally insulated box, and a polymer film (Figure 15A). The r-PET textile showed the lowest values due to its transmittance/emittance in the mid-infrared (MIR) spectrum and its low thermal conductivity. As depicted in Figure 15B, a significant amount of thermal energy was trapped in the space between the microheater and the textile, resulting in a temperature of 28.46 °C, which is 6.8 °C lower than that of the skin alone. This suggests that the thermal comfort of the human body may be reduced when using the untreated r-PET textile.

The r-PET/TiO_2 textile showed the second lowest temperature value, with an average of 28.84 °C, reaffirming the role of aggregates in preventing infrared light from passing through the textile. The r-PET/TiO_2-GO 5:1 and r-PET/TiO_2-GO 1:1 textiles showed the smallest temperature differences relative to the simulated skin alone, with differences of 1.27 and 3.79 °C, respectively. The lower thermal performance of the 1:1 molar ratio formulation may be a consequence of the wider spacing of fibers, leaving similar zones at similar wavelengths in the MIR spectrum (Figure 9C). Considering the thermal conductivity and transmittance/emittance data in the AW, along with their similar indoor performance, it can be concluded that the r-PET/TiO_2-GO 5:1 textile provides the best cooling characteristics.

It is important to note that the thermal performance of the textiles developed in this study could be enhanced by altering their orientation. In the experimental protocol, the fabrics were consistently positioned to face the sky. However, in practical applications, textiles are typically oriented vertically, which has been found to increase exposure to terrestrial heat, thereby reducing thermal comfort due to a decreased cooling efficiency. Employing materials with selective emissivity in AW wavelengths could further amplify the temperature differential between the textiles and the control samples, both indoors and outdoors. This is because the heat gain in the textiles due to terrestrial radiation is significantly reduced, as it is limited to AW wavelengths rather than the broadband spectrum. Consequently, the radiative heat loss from the textiles is less likely to be surpassed, resulting in improved relative cooling.[100]

https://doi.org/10.1021/acsomega.4c05600
ACS Omega 2024, 9, 49143−49162

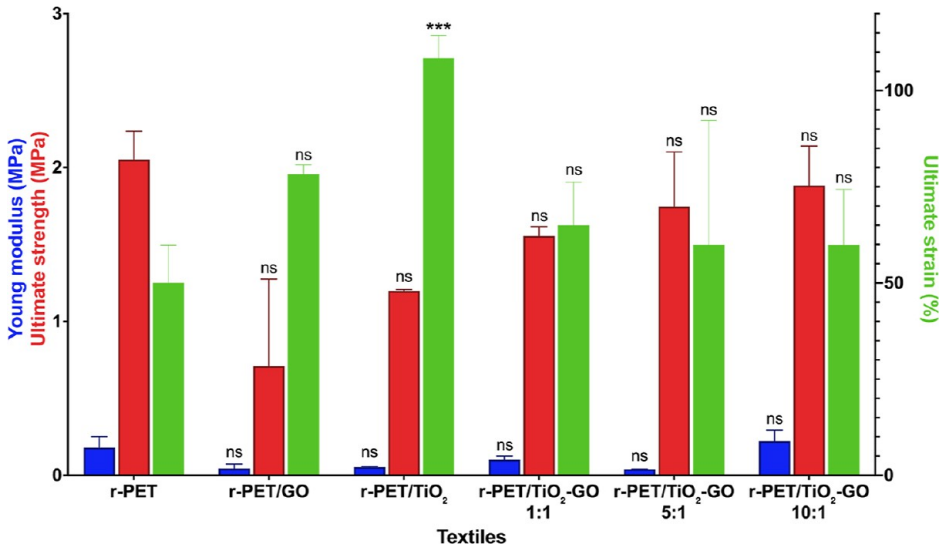

Figure 16. Mechanical properties of r-PET, r-PET/GO, r-PET/TiO_2, r-PET/TiO_2-GO 1:1, r-PET/TiO_2-GO 5:1, and r-PET/TiO_2-GO 10:1 textiles.

Table 3. Mean Young's Modulus, Tensile Strength, and Ultimate Strain of r-PET, r-PET/GO, r-PET/TiO_2, r-PET/TiO_2-GO 1:1, r-PET/TiO_2-GO 5:1, and r-PET/TiO_2-GO 10:1 Textiles with Standard Deviation

	r-PET	r-PET/GO	r-PET/TiO_2	r-PET/TiO_2-GO 1:1	r-PET/TiO_2-GO 5:1	r-PET/TiO_2-GO 10:1
Young modulus (MPa)	0.179 ± 0.070	0.044 ± 0.028	0.053 ± 0.005	0.101 ± 0.023	0.040 ± 0.001	0.222 ± 0.071
tensile strength (MPa)	2.051 ± 0.185	0.710 ± 0.567	1.198 ± 0.008	1.555 ± 0.061	1.746 ± 0.355	1.883 ± 0.255
ultimate strain (%)	50.088 ± 9.773	78.318 ± 2.389	108.401 ± 5.880	64.991 ± 11.170	59.912 ± 32.361	59.894 ± 14.443

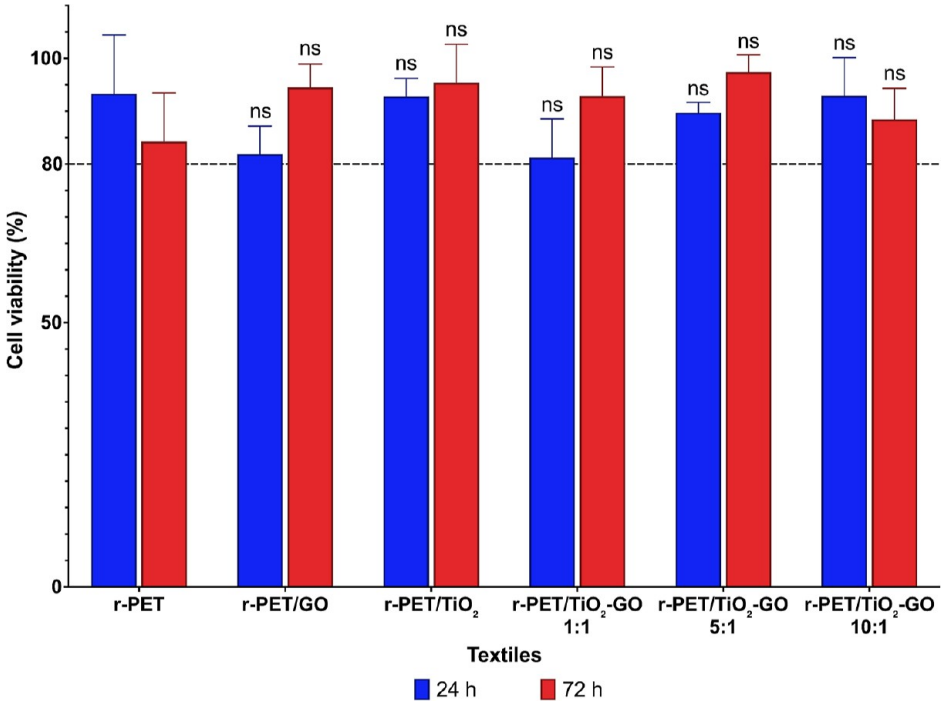

Figure 17. Cell viability of r-PET, r-PET/GO, r-PET/TiO_2, r-PET/TiO_2-GO 1:1, r-PET/TiO_2-GO 5:1, and r-PET/TiO_2-GO 10:1 textiles at 24 and 72 h.

3.2.6. Textile System Mechanical Properties. The mechanical properties of the textiles are shown in Figure 16 and Table 3. In most cases, no significant statistical differences were observed between r-PET and the other experimental groups regarding Young's modulus, tensile strength, and ultimate strain. Notable changes were seen in the Young's modulus for the r-PET and r-PET/GO groups and in the ultimate strain for the r-PET and r-PET/TiO_2 fabrics. For GO, it has been shown that at concentrations higher than 1% (w/w), there can be a reduction in Young's modulus compared to r-PET. This is due

https://doi.org/10.1021/acsomega.4c05600
ACS Omega 2024, 9, 49143−49162

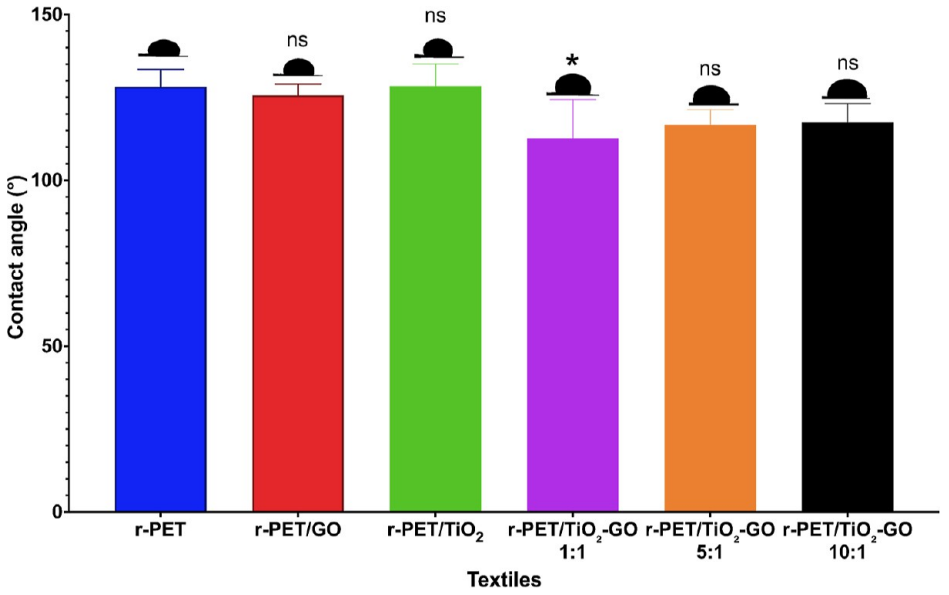

Figure 18. Water contact angles of r-PET, r-PET/GO, r-PET/TiO_2, r-PET/TiO_2-GO 1:1, r-PET/TiO_2-GO 5:1, and r-PET/TiO_2-GO 10:1 textiles.

to the dispersion of high concentrations of nanolayers, which tend to adopt a wrinkled structure that inflates rather than stretches when stresses are applied to the textiles.[83] The increase in ultimate strain for the r-PET/TiO_2 sample occurs because the nanoparticles tend to absorb some of the energy, helping to reduce failure propagation[101,102] and thus delaying the rupture of the textile.

3.2.7. Textile System Cell Viability. The toxicity of the textiles was evaluated in an in vitro model using the human skin keratinocyte cell line HaCaT. The viability of HaCaT cells was assessed using the MTT assay at 24 and 72 h (Figure 17). The study shows that no textile reveals a cell viability lower than 80% after the evaluated times, which is within the limits accepted by ISO 10993 standard. This result is attributed to the high biocompatibility of GO at low weight percentages in electrospinning systems.[103]

3.2.8. Textile System Usability. The contact angles of the textile formulations are shown in Figure 18. The hydrophobic character of r-PET presents a slight decrease from 128.3 to 125.7° when GO is included, due to the hydrophilic nature of its oxygenated groups.[86] TiO_2 NPs generate an increase in the contact angle due to their hydrophobicity.[101] As the molar ratio between TiO_2 NPs and GO increases, the contact angle also increases from 112.7 to 117.5°. However, the contact angles are found to be greater than 110°, enhancing the self-cleaning properties of the textiles.[18]

4. CONCLUSIONS

In summary, this study successfully manufactured, characterized, and evaluated a nanocomposite polymeric textile system incorporating recycled poly(ethylene terephthalate) (r-PET) and GO modified with titanium dioxide nanoparticles (TiO_2 NPs). The textile system demonstrates exceptional thermal properties, owing to the high refractive capabilities of TiO_2 NPs, the conductive properties of GO nanolayers, and the infrared transparency of the r-PET polymer. These attributes collectively enhance the dissipation of thermal energy in both indoor and outdoor environments. The results indicate that the textile with a 5:1 molar ratio between TiO_2 NPs and GO exhibits superior performance, promoting SS wavelength reflectance at a value of 89.26% and effectively preventing solar rays from penetrating the skin through the fabric. The textile also demonstrates an AW transmittance/emittance percentage of 98.40% and a thermal conductivity index of 0.66 W/m K, emphasizing its efficiency in dissipating heat within the infrared spectrum. The developed formulation maintains the human body at a temperature 20.06 °C lower than the skin in outdoor settings and 1.27 °C lower indoors, making it an excellent candidate for preventing HRI episodes. Additionally, the interaction between the nanoconjugate and the polymer sustains the mechanical properties of the textile and retains high contact angles close to 120°, which enhances the self-cleaning properties of the fabric. Biological tests confirm that the developed fibers do not adversely affect skin cells, maintaining high cell viability percentages and validating their safe use on epithelial cells without posing health risks. This work presents an environmentally friendly and promising methodology for the large-scale production of high-performance sports cooling fabrics, providing a potent and technically sound solution for enhancing thermal comfort and safety in athletic applications.

AUTHOR INFORMATION

Corresponding Author

Ian C. Orjuela-Garzón − *Department of Biomedical Engineering, Universidad de los Andes, Bogotá 111711, Colombia;* orcid.org/0009-0000-4306-2197; Email: ic.orjuela@uniandes.edu.co

Authors

Cristian F. Rodríguez − *Department of Biomedical Engineering, Universidad de los Andes, Bogotá 111711, Colombia; Neuroscience Group of Antioquia, Cellular and Molecular Neurobiology Area, School of Medicine, SIU, Universidad de Antioquia, Medellín 050010, Colombia;* orcid.org/0000-0002-6617-0534

Juan C. Cruz − *Department of Biomedical Engineering, Universidad de los Andes, Bogotá 111711, Colombia; Grupo de Diseño de Productos y Procesos (GDPP), Department of Chemical and Food Engineering, Universidad de los Andes,*

https://doi.org/10.1021/acsomega.4c05600
ACS Omega 2024, 9, 49143−49162

Bogotá 111711, Colombia; orcid.org/0000-0002-7790-7546

Juan C. Briceño − *Department of Biomedical Engineering, Universidad de los Andes, Bogotá 111711, Colombia; Department of Congenital Heart Disease and Cardiovascular Surgery, Fundación CardioInfantil Instituto de Cardiología, Bogotá 110131, Colombia*

Complete contact information is available at: https://pubs.acs.org/10.1021/acsomega.4c05600

Author Contributions

IO-G: conceptualization, data curation, formal analysis, investigation, methodology, project administration, software, validation, visualization, writing—original draft. CR: data curation, formal analysis, investigation, methodology, software, visualization, writing—original draft. JC: conceptualization, project administration, supervision, validation, writing—review and editing. JB: conceptualization, project administration, resources, supervision, validation, writing—review and editing.

Notes

The authors declare no competing financial interest.

■ ACKNOWLEDGMENTS

The authors extend their gratitude to Biomedical Engineering, Civil and Environmental Engineering, Chemical and Food Engineering, Mechanical Engineering, Electric and Electronic Engineering, and Physics departments at Universidad de los Andes (Bogota, Colombia). The authors also appreciate technical assistance with SEM microscopy imaging from the μ-Core Facility at Universidad de los Andes. Special thanks to María Alejandra Rodríguez, Valentina Quezada, and Valentina Jaramillo for their assistance in the nanoconjugate development and the biological testing and to Julieth Monroy for providing the necessary elements and spaces to carry out the thermal conductivity assembly and the indoor and outdoor measurements.

■ REFERENCES

(1) Puley, G. *Extreme Heat: Preparing for the Heat Waves of the Future*: New York, 2022.

(2) Odonkor, S. T.; Adams, S. Climate Change-Mediated Heat Stress Vulnerability and Adaptation Strategies among Outdoor Workers. *Clim. Dev.* **2022**, *14* (7), 591−599.

(3) Yi, F.; Zhou, T.; Yu, L.; McCarl, B.; Wang, Y.; Jiang, F.; Wang, Y. Outdoor Heat Stress and Cognition: Effects on Those over 40 Years Old in China. *Weather Clim. Extrem.* **2021**, *32*, 100308.

(4) Hollander, K.; Klöwer, M.; Richardson, A.; Navarro, L.; Racinais, S.; Scheer, V.; Murray, A.; Branco, P.; Timpka, T.; Junge, A.; Edouard, P. Apparent Temperature and Heat-related Illnesses during International Athletic Championships: A Prospective Cohort Study. *Scand. J. Med. Sci. Sports* **2021**, *31* (11), 2092−2102.

(5) Yeargin, S. W.; Dompier, T. P.; Casa, D. J.; Hirschhorn, R. M.; Kerr, Z. Y. Epidemiology of Exertional Heat Illnesses in National Collegiate Athletic Association Athletes During the 2009−2010 Through 2014−2015 Academic Years. *J. Athl. Train.* **2019**, *54* (1), 55−63.

(6) Alkemade, P.; Daanen, H. A. M.; Janssen, T. W. J.; Broad, E.; Goosey-Tolfrey, V. L.; Ibusuki, T.; Kneepkens, H.; Périard, J. D.; Eijsvogels, T. M. H. Heat Preparedness and Exertional Heat Illness in Paralympic Athletes: A Tokyo 2020 Survey. *Temperature* **2023**, *10* (2), 264−275.

(7) Ebi, K. L.; Capon, A.; Berry, P.; Broderick, C.; de Dear, R.; Havenith, G.; Honda, Y.; Kovats, R. S.; Ma, W.; Malik, A.; Morris, N. B.; Nybo, L.; Seneviratne, S. I.; Vanos, J.; Jay, O. Hot Weather and Heat Extremes: Health Risks. *Lancet* **2021**, *398* (10301), 698−708.

(8) Walter, E.; Steel, K. Management of Exertional Heat Stroke: A Practical Update for Primary Care Physicians. *Br. J. Gen. Pract.* **2018**, *68* (668), 153−154.

(9) Peng, Y.; Chen, J.; Song, A. Y.; Catrysse, P. B.; Hsu, P.-C.; Cai, L.; Liu, B.; Zhu, Y.; Zhou, G.; Wu, D. S.; Lee, H. R.; Fan, S.; Cui, Y. Nanoporous Polyethylene Microfibres for Large-Scale Radiative Cooling Fabric. *Nat. Sustain.* **2018**, *1* (2), 105−112.

(10) Song, Y.-N.; Li, Y.; Yan, D.-X.; Lei, J.; Li, Z.-M. Novel Passive Cooling Composite Textile for Both Outdoor and Indoor Personal Thermal Management. *Composites, Part A* **2020**, *130*, 105738−105739.

(11) Ullah, H. M. K.; Lejeune, J.; Cayla, A.; Monceaux, M.; Campagne, C.; Devaux, E. ·. A Review of Noteworthy/Major Innovations in Wearable Clothing for Thermal and Moisture Management from Material to Fabric Structure. *Text. Res. J.* **2022**, *92* (17−18), 3351−3386.

(12) Gorji, M.; Mazinani, S.; Gharehaghaji, A. A. A Review on Emerging Developments in Thermal and Moisture Management by Membrane-based Clothing Systems towards Personal Comfort. *J. Appl. Polym. Sci.* **2022**, *139* (27), 1−27.

(13) Peng, Y.; Lee, H. K.; Wu, D. S.; Cui, Y. Bifunctional Asymmetric Fabric with Tailored Thermal Conduction and Radiation for Personal Cooling and Warming. *Engineering* **2022**, *10*, 167−173.

(14) Peng, L.; Su, B.; Yu, A.; Jiang, X. Review of Clothing for Thermal Management with Advanced Materials. *Cellulose* **2019**, *26* (11), 6415−6448.

(15) Chen, M.; Liu, Y.; Zhao, X. Emerging Passive Thermoregulatory Textiles through Tailoring Different Heat Transfer Routes. *Text. Res. J.* **2023**, *93* (13−14), 3414−3439.

(16) Zhang, X. A.; Yu, S.; Xu, B.; Li, M.; Peng, Z.; Wang, Y.; Deng, S.; Wu, X.; Wu, Z.; Ouyang, M.; Wang, Y. Dynamic Gating of Infrared Radiation in a Textile. *Science* **2019**, *363* (6427), 619−623.

(17) Lee, J.; Sul, H.; Lee, W.; Pyun, K. R.; Ha, I.; Kim, D.; Park, H.; Eom, H.; Yoon, Y.; Jung, J.; Lee, D.; Ko, S. H. Stretchable Skin-Like Cooling/Heating Device for Reconstruction of Artificial Thermal Sensation in Virtual Reality. *Adv. Funct. Mater.* **2020**, *30* (29), 1909171.

(18) Li, M.; Zhang, M.; Mahar, F. K.; Wei, L.; Wang, Z.; Wang, X.; Wei, K. Fabrication of Fibrous Nanofiber Membranes for Passive Radiation Cooling. *J. Mater. Sci.* **2022**, *57* (33), 16080−16090.

(19) Song, Y.; Lei, M.; Lei, J.; Li, Z. A Scalable Hybrid Fiber and Its Textile with Pore and Wrinkle Structures for Passive Personal Cooling. *Adv. Mater. Technol.* **2020**, *5* (7), 1−9.

(20) Wu, X.; Li, J.; Jiang, Q.; Zhang, W.; Wang, B.; Li, R.; Zhao, S.; Wang, F.; Huang, Y.; Lyu, P.; Zhao, Y.; Zhu, J.; Zhang, R. An All-Weather Radiative Human Body Cooling Textile. *Nat. Sustain.* **2023**, *6* (11), 1446−1454.

(21) Miao, D.; Wang, X.; Yu, J.; Ding, B. Nanoengineered Textiles for Outdoor Personal Cooling and Drying. *Adv. Funct. Mater.* **2022**, *32*, 1−30.

(22) Mandal, J.; Fu, Y.; Overvig, A. C.; Jia, M.; Sun, K.; Shi, N. N.; Zhou, H.; Xiao, X.; Yu, N.; Yang, Y. Hierarchically Porous Polymer Coatings for Highly Efficient Passive Daytime Radiative Cooling. *Science* **2018**, *362* (6412), 315−319.

(23) Wong, A.; Daoud, W. A.; Liang, H.; Szeto, Y. S. Application of Rutile and Anatase onto Cotton Fabric and Their Effect on the NIR Reflection/Surface Temperature of the Fabric. *Sol. Energy Mater. Sol. Cells* **2015**, *134*, 425−437.

(24) Mehrizi, M. K.; Mortazavi, S. M.; Mallakpour, S.; Bidoki, S. M. The Effect of Nano- and Micro-TiO2 Particles on Reflective Behavior of Printed Cotton/Nylon Fabrics in Vis/NIR Regions. *Color Res. Appl.* **2012**, *37* (3), 199−205.

(25) Shams-Nateri, A.; Kazemian, S.; Piri, N. Nano-TiO2 Coated Cotton Fabrics with Temperature Regulating Properties. *J. Textil. Inst.* **2020**, *111* (8), 1223−1230.

(26) Liang, Z.; Zhou, Z.; Li, J.; Zhang, S.; Dong, B.; Zhao, L.; Wu, C.; Yang, H.; Chen, F.; Wang, S. Multi-Functional Silk Fibers/Fabrics

with a Negligible Impact on Comfortable and Wearability Properties for Fiber Bulk. *Chem. Eng. J.* **2021**, *415*, 128980−128989.
(27) Zeng, S.; Pian, S.; Su, M.; Wang, Z.; Wu, M.; Liu, X.; Chen, M.; Xiang, Y.; Wu, J.; Zhang, M.; Cen, Q.; Tang, Y.; Zhou, X.; Huang, Z.; Wang, R.; Tunuhe, A.; Sun, X.; Xia, Z.; Tian, M.; Chen, M.; Ma, X.; Yang, L.; Zhou, J.; Zhou, H.; Yang, Q.; Li, X.; Ma, Y.; Tao, G. Hierarchical-Morphology Metafabric for Scalable Passive Daytime Radiative Cooling. *Science* **2021**, *373* (6555), 692−696.
(28) Qiu, S.; Jia, H.; Jiang, S. Fabrication and Characterization of Thermal Management Fabric with Heating and Cooling Modes through Magnetron Sputtering. *Mater. Lett.* **2021**, *300*, 130217−130224.
(29) Bonetti, L.; Fiorati, A.; Serafini, A.; Masotti, G.; Tana, F.; D'Agostino, A.; Draghi, L.; Altomare, L.; Chiesa, R.; Farè, S.; Bianchi, M.; Rizzi, L. G.; De Nardo, L. Graphene Nanoplatelets Composite Membranes for Thermal Comfort Enhancement in Performance Textiles. *J. Appl. Polym. Sci.* **2021**, *138* (2), 1−10.
(30) Guo, Y.; Dun, C.; Xu, J.; Mu, J.; Li, P.; Gu, L.; Hou, C.; Hewitt, C. A.; Zhang, Q.; Li, Y.; Carroll, D. L.; Wang, H. Ultrathin, Washable, and Large-Area Graphene Papers for Personal Thermal Management. *Small* **2017**, *13* (44), 1−9.
(31) Xie, A.; Zhu, L.; Liang, Y.; Mao, J.; Liu, Y.; Chen, S. Fiber-spinning Asymmetric Assembly for Janus-structured Bifunctional Nanofiber Films towards All-Weather Smart Textile. *Angew. Chem., Int. Ed.* **2022**, *61* (40), 1−8.
(32) Gorji, M.; Karimi, M.; Rahimi Larki, M.; Safavi, A. Theoretical Modeling of Thermal Stress Imposed by Selective Permeation Membranes Reinforced with Graphene Oxide. *J. Appl. Polym. Sci.* **2017**, *134* (17), 1−10.
(33) Tabor, J.; Chatterjee, K.; Ghosh, T. K. Smart Textile-Based Personal Thermal Comfort Systems: Current Status and Potential Solutions. *Adv. Mater. Technol.* **2020**, *5* (5), 1901155.
(34) Rivero, P. J.; Urrutia, A.; Goicoechea, J.; Arregui, F. J. Nanomaterials for Functional Textiles and Fibers. *Nanoscale Res. Lett.* **2015**, *10* (1), 501.
(35) Majumdar, A.; Shukla, S.; Singh, A. A.; Arora, S. Circular Fashion: Properties of Fabrics Made from Mechanically Recycled Poly-Ethylene Terephthalate (PET) Bottles. *Resour. Conserv. Recycl.* **2020**, *161*, 104915.
(36) Sousa, S. R. C. A.; Silva, T. E. D.; Aguiar, L. C.; Silva, K. K. O. S.; Leite, A. M. D. The Impact of PET Fiber on the Textile Industry: Review and Perspectives on Sustainability between 2000 and 2020. *International Symposium "Technical Textiles-Present and Future"*; Sciendo, 2022; pp 166−172.
(37) Boriskina, S. V. An Ode to Polyethylene. *MRS Energy Sustain.* **2019**, *6* (1), 14.
(38) Lei, M.; Psikuta, A.; Liu, Y.; Rossi, R. M.; Li, Y. A. A numerical approach to evaluate the personal radiative thermal management of textiles part one: Mid-infrared transmittance, reflection and absorption. *Results Phys.* **2022**, *43*, 106043.
(39) Kahraman Döğüşcü, D.; Kızıl, C.¸.; Biçer, A.; Sarı, A.; Alkan, C. Microencapsulated n -Alkane Eutectics in Polystyrene for Solar Thermal Applications. *Sol. Energy* **2018**, *160*, 32−42.
(40) Gu, B.; Zhou, H.; Zhang, Z.; Zhang, T.; Chen, M.; Qiu, F.; Yang, D. Cellulose-Based Hybrid Membrane with Functional Integration for Personal Thermal Management Applications. *Appl. Surf. Sci.* **2021**, *535*, 147670−147678.
(41) Luo, H.; Zhu, Y.; Xu, Z.; Hong, Y.; Ghosh, P.; Kaur, S.; Wu, M.; Yang, C.; Qiu, M.; Li, Q. Outdoor Personal Thermal Management with Simultaneous Electricity Generation. *Nano Lett.* **2021**, *21* (9), 3879−3886.
(42) Li, D.; Liang, X.; Li, S.; Wang, T.; Han, G.; Guo, Z. Bioinspired Textile with Dual-Stimuli Responsive Wettability for Body Moisture Management and Signal Expression. *New J. Chem.* **2021**, *45* (27), 12193−12202.
(43) Xie, X.; Liu, Y.; Zhu, Y.; Xu, Z.; Liu, Y.; Ge, D.; Yang, L. Enhanced IR Radiative Cooling of Silver Coated PA Textile. *Polymers* **2021**, *14* (1), 147−148.
(44) Kizildag, N. Smart Composite Nanofiber Mats with Thermal Management Functionality. *Sci. Rep.* **2021**, *11* (1), 4256−4316.
(45) Jung, Y.; Jeong, S.; Ahn, J.; Lee, J.; Ko, S. H. High Efficiency Breathable Thermoelectric Skin Using Multimode Radiative Cooling/Solar Heating Assisted Large Thermal Gradient. *Small* **2024**, *20* (1), 2308572.
(46) Pyun, K. R.; Jeong, S.; Yoo, M. J.; Choi, S. H.; Baik, G.; Lee, M.; Song, J.; Ko, S. H. Tunable Radiative Cooling by Mechanochromic Electrospun Micro-Nanofiber Matrix. *Small* **2024**, *20* (20), 2308572.
(47) Patarroyo, J. L.; Cifuentes, J.; Muñoz, L. N.; Cruz, J. C.; Reyes, L. H. Novel Antibacterial Hydrogels Based on Gelatin/Polyvinyl-Alcohol and Graphene Oxide/Silver Nanoconjugates: Formulation, Characterization, and Preliminary Biocompatibility Evaluation. *Heliyon* **2022**, *8* (3), No. e09145.
(48) Singh, A. R.; Deshpande, V. D. Preparation and Characterization of Solution Cast Films of PET Reorganized PET and Their MWNT Nanocomposites. *AIP Conf. Proc.* **2013**, *1538*, 190−195.
(49) Rodríguez, C. F.; Guzmán-Sastoque, P.; Muñoz-Camargo, C.; Reyes, L. H.; Osma, J. F.; Cruz, J. C. Enhancing Magnetic Micro- and Nanoparticle Separation with a Cost-Effective Microfluidic Device Fabricated by Laser Ablation of PMMA. *Micromachines* **2024**, *15* (8), 1057.
(50) Rodríguez, C. F.; Guzmán-Sastoque, P.; Gantiva-Diaz, M.; Gómez, S. C.; Quezada, V.; Muñoz-Camargo, C.; Osma, J. F.; Reyes, L. H.; Cruz, J. C. Low-Cost Inertial Microfluidic Device for Microparticle Separation: A Laser-Ablated PMMA Lab-on-a-Chip Approach without a Cleanroom. *HardwareX* **2023**, *16*, No. e00493.
(51) Ortegón, S.; Peñaranda, P. A.; Rodríguez, C. F.; Noguera, M. J.; Florez, S. L.; Cruz, J. C.; Rivas, R. E.; Osma, J. F. Magnetic Torus Microreactor as a Novel Device for Sample Treatment via Solid-Phase Microextraction Coupled to Graphite Furnace Atomic Absorption Spectroscopy: A Route for Arsenic Pre-Concentration. *Molecules* **2022**, *27* (19), 6198.
(52) Rodríguez, C. F.; Báez-Suárez, M.; Muñoz-Camargo, C.; Reyes, L. H.; Osma, J. F.; Cruz, J. C. Zweifach−Fung Microfluidic Device for Efficient Microparticle Separation: Cost-Effective Fabrication Using CO2 Laser-Ablated PMMA. *Micromachines* **2024**, *15* (7), 932.
(53) Fuentes Melo, L. F. *Microheater for Microfluidic Systems*; Universidad De Los Andes: Bogotá, 2022.
(54) Rodríguez-Soto, M. A.; Riveros-Cortés, A.; Orjuela-Garzón, I. C.; Fernández-Calderón, I. M.; Rodríguez, C. F.; Vargas, N. S.; Ostos, C.; Camargo, C. M.; Cruz, J. C.; Kim, S.; D'Amore, A.; Wagner, W. R.; Briceño, J. C. Redefining Vascular Repair: Revealing Cellular Responses on PEUU—Gelatin Electrospun Vascular Grafts for Endothelialization and Immune Responses on in Vitro Models. *Front. Bioeng. Biotechnol.* **2024**, *12*, 1410863.
(55) Rodriguez, C. F.; Ortiz, C. L.; Giraldo, R. K. A.; Munoz, C. C.; Cruz, J. C. In Silico Study of Spheroids Fusion through Magnetic Field Gradients. *2021 IEEE 2nd International Congress of Biomedical Engineering and Bioengineering (CI-IB&BI)*; IEEE, 2021, pp 1−9.
(56) Al-Amin, M.; Chandra Dey, S.; Ur Rashid, T.; Ashaduzzaman, Md.; Shamsuddin, S. M. Solar Assisted Photocatalytic Degradation of Reactive Azo Dyes in Presence of Anatase Titanium Dioxide. *Int. J. Res. Eng. Technol.* **2016**, *2* (3), 14−21.
(57) Al-Oubidy, E. A.; Kadhim, F. J. Photocatalytic Activity of Anatase Titanium Dioxide Nanostructures Prepared by Reactive Magnetron Sputtering Technique. *Opt. Quantum Electron.* **2019**, *51* (1), 23.
(58) Dalod, A. R. M.; Henriksen, L.; Grande, T.; Einarsrud, M.-A. Functionalized TiO2 Nanoparticles by Single-Step Hydrothermal Synthesis: The Role of the Silane Coupling Agents. *Beilstein J. Nanotechnol.* **2017**, *8*, 304−312.
(59) Cheng, F.; Sajedin, S. M.; Kelly, S. M.; Lee, A. F.; Kornherr, A. UV-Stable Paper Coated with APTES-Modified P25 TiO2 Nanoparticles. *Carbohydr. Polym.* **2014**, *114*, 246−252.
(60) Ognjanović, M.; Stanković, V.; Knežević, S.; Antić, B.; Vranješ-Djurić, S.; Stanković, D. M. TiO2/APTES Cross-Linked to

https://doi.org/10.1021/acsomega.4c05600
ACS Omega 2024, 9, 49143−49162

Carboxylic Graphene Based Impedimetric Glucose Biosensor. *Microchem. J.* **2020**, *158*, 105150.
(61) Ullah, R.; Khan, S. A.; Aladresi, A. A. M.; Alharbi, S. A.; Chinnathambi, A. Ovalbumin-Mediated Synthesis and Simultaneous Functionalization of Graphene with Increased Protein Stability. *Green Chem. Lett. Rev.* **2020**, *13* (1), 60−67.
(62) Sharma, N.; Sharma, V.; Jain, Y.; Kumari, M.; Gupta, R.; Sharma, S. K.; Sachdev, K. Synthesis and Characterization of Graphene Oxide (GO) and Reduced Graphene Oxide (RGO) for Gas Sensing Application. *Macromol. Symp.* **2017**, *376* (1), 1700006.
(63) Ameer, S.; Gul, I. H. Influence of Reduced Graphene Oxide on Effective Absorption Bandwidth Shift of Hybrid Absorbers. *PLoS One* **2016**, *11* (6), No. e0153544.
(64) Céspedes-Valenzuela, D. N.; Sánchez-Rentería, S.; Cifuentes, J.; Gantiva-Diaz, M.; Serna, J. A.; Reyes, L. H.; Ostos, C.; Cifuentes-De la Portilla, C.; Muñoz-Camargo, C.; Cruz, J. C. Preparation and Characterization of an Injectable and Photo-Responsive Chitosan Methacrylate/Graphene Oxide Hydrogel: Potential Applications in Bone Tissue Adhesion and Repair. *Polymers* **2022**, *14* (1), 126.
(65) Nath, B. C.; Das, D.; Kamrupi, I. R.; Mohan, K. J.; Ahmed, G. A.; Dolui, S. K. An Efficient Quasi Solid State Dye Sensitized Solar Cell Based on Polyethylene Glycol/Graphene Nanosheet Gel Electrolytes. *RSC Adv.* **2015**, *5* (115), 95385−95393.
(66) Deb, A.; Vimala, R. Camptothecin Loaded Graphene Oxide Nanoparticle Functionalized with Polyethylene Glycol and Folic Acid for Anticancer Drug Delivery. *J. Drug Deliv. Sci. Technol.* **2018**, *43*, 333−342.
(67) Almeida, N. A.; Martins, P. M.; Teixeira, S.; Lopes da Silva, J. A.; Sencadas, V.; Kühn, K.; Cuniberti, G.; Lanceros-Mendez, S.; Marques, P. A. A. P. TiO2/Graphene Oxide Immobilized in P(VDF-TrFE) Electrospun Membranes with Enhanced Visible-Light-Induced Photocatalytic Performance. *J. Mater. Sci.* **2016**, *51* (14), 6974−6986.
(68) Wang, C.; Mao, H.; Wang, C.; Fu, S. Dispersibility and Hydrophobicity Analysis of Titanium Dioxide Nanoparticles Grafted with Silane Coupling Agent. *Ind. Eng. Chem. Res.* **2011**, *50* (21), 11930−11934.
(69) Tayel, A.; Ramadan, A.; El Seoud, O. Titanium Dioxide/Graphene and Titanium Dioxide/Graphene Oxide Nanocomposites: Synthesis, Characterization and Photocatalytic Applications for Water Decontamination. *Catalysts* **2018**, *8* (11), 491.
(70) Souza, T. G. F.; Ciminelli, V. S. T.; Mohallem, N. D. S. A Comparison of TEM and DLS Methods to Characterize Size Distribution of Ceramic Nanoparticles. *J. Phys. Conf. Ser.* **2016**, *733*, 012039.
(71) Kaniyoor, A.; Ramaprabhu, S. A Raman Spectroscopic Investigation of Graphite Oxide Derived Graphene. *AIP Adv.* **2012**, *2* (3), 032183.
(72) Al-Taweel, S.; Saud, H. New Route for Synthesis of Pure Anatase TiO2 Nanoparticles via Utrasound-Assisted Sol-Gel Method. *J. Chem. Pharm. Res.* **2016**, *8* (2), 620−626.
(73) Xavier, J. R. Graphene Oxide/Metal Sulfide and Oxide Nanocomposite Electrodes for High Electrochemical Performance Supercapacitor Applications. *J. Mater. Eng. Perform.* **2024**, *33*, 1772−1785.
(74) Balarak, D.; Mengelizadeh, N.; Rajiv, P.; Chandrika, K. Photocatalytic Degradation of Amoxicillin from Aqueous Solutions by Titanium Dioxide Nanoparticles Loaded on Graphene Oxide. *Environ. Sci. Pollut. Res.* **2021**, *28* (36), 49743−49754.
(75) Boroujerdi, R.; Paul, R. Introducing Graphene−Indium Oxide Electrochemical Sensor for Detecting Ethanol in Aqueous Samples with CCD-RSM Optimization. *Chemosensors* **2022**, *10* (2), 42.
(76) Zuas, O.; Budiman, H. Synthesis of Nanostructured Copper-Doped Titania and Its Properties. *Nano-Micro Lett.* **2013**, *5* (1), 26−33.
(77) Sundaran, S. P.; Reshmi, C. R.; Sagitha, P.; Sujith, A. Polyurethane Nanofibrous Membranes Decorated with Reduced Graphene Oxide−TiO2 for Photocatalytic Templates in Water Purification. *J. Mater. Sci.* **2020**, *55* (14), 5892−5907.
(78) Anandhi, P.; Harikrishnan, S.; Senthil Kumar, V. J.; Lai, W.-C.; Mahmoud, A. E. D. The Enhanced Energy Density of RGO/TiO2 Based Nanocomposite as Electrode Material for Supercapacitor. *Electronics* **2022**, *11* (11), 1792.
(79) Hassan, M. M.; Mahmoud, G.. A.; Ali, M. A.; Hegazy, E. A. Thermal and Morphological Behavior of Irradiated Composite Materials Based on Injection-moulded Recycled Polyethylene Terephthalate. *J. Appl. Polym. Sci.* **2008**, *107* (6), 3974−3980.
(80) Alshammari, B. A.; Al-Mubaddel, F. S.; Karim, M. R.; Hossain, M.; Al-Mutairi, A. S.; Wilkinson, A. N. Addition of Graphite Filler to Enhance Electrical, Morphological, Thermal, and Mechanical Properties in Poly (Ethylene Terephthalate): Experimental Characterization and Material Modeling. *Polymers* **2019**, *11* (9), 1411.
(81) Chen, C.-W.; Liu, P.-H.; Lin, F.-J.; Cho, C.-J.; Wang, L.-Y.; Mao, H.-I.; Chiu, Y.-C.; Chang, S.-H.; Rwei, S.-P.; Kuo, C.-C. Influence of Different Molecular Weights and Concentrations of Poly(Glycidyl Methacrylate) on Recycled Poly(Ethylene Terephthalate): A Thermal, Mechanical, and Rheological Study. *J. Polym. Environ.* **2020**, *28* (11), 2880−2892.
(82) Evgenidou, E.; Ainali, N. M.; Rapti, A.; Bikiaris, R. D.; Nannou, C.; Lambropoulou, D. A. Photocatalytic Performance of Buoyant TiO2-Immobilized Poly(Ethylene Terephthalate) Beads for the Removal of the Anticonvulsant Drug Pregabalin from Water and Leachate. *J. Environ. Chem. Eng.* **2023**, *11* (5), 110697.
(83) Barbosa, M. C.; Razzino, C. d. A.; Stocco, T. D.; Santana, M.; Ghosh, A.; Pereira, L. F.; Tierra-Criollo, C. J.; Lobo, A. O.; Lobo, A. O. Production of RGO-Based Electrospinning Nanocomposites Incorporated in Recycled PET as an Alternative Dry Electrode. *Polymers* **2022**, *14* (20), 4288.
(84) Kalaoglu-Altan, O. I.; Karagüzel Kayaoğlu, B.; Trabzon, L. Fabrication and Characterization of Graphene-loaded Recycled Poly(Ethylene Terephthalate) Electrospun Composite Nanofibrous Mats with Improved Thermal Conductivity. *Polym. Compos.* **2024**, *45*, 709.
(85) Huang, C.-L.; Wu, H.-H.; Jeng, Y.-C.; Liang, W.-Z. Electrospun Graphene Nanosheet-Filled Poly(Trimethylene Terephthalate) Composite Fibers: Effects of the Graphene Nanosheet Content on Morphologies, Electrical Conductivity, Crystallization Behavior, and Mechanical Properties. *Polymers* **2019**, *11* (1), 164.
(86) Selatile, K.; Ray, S. S.; Ojijo, V.; Sadiku, R. E. Morphological, Thermal, and Mechanical Properties of Electrospun Recycled Poly(Ethylene Terephthalate)/Graphene Oxide Composite Nanofiber Membranes. *ACS Omega* **2021**, *6* (32), 21005−21015.
(87) Song, J.; Zhao, Q.; Meng, C.; Meng, J.; Chen, Z.; Li, J. Hierarchical Porous Recycled PET Nanofibers for High-Efficiency Aerosols and Virus Capturing. *ACS Appl. Mater. Interfaces* **2021**, *13* (41), 49380−49389.
(88) Nooh, N.; Salim, R. M..; Reusmaazran Yusof, M..; Wan, K. W. A. K. Fabrication and Characterisation of Recycled Polyethylene Terephthalate/Graphene Oxide Nanofibres as a Potential Adsorbent for Methylene Blue. *Malays. J. Biochem. Mol. Biol.* **2022**, *24* (2), 158−165.
(89) Liu, K.; Deng, L.; Zhang, T.; Shen, K.; Wang, X. Facile Fabrication of Environmentally Friendly, Waterproof, and Breathable Nanofibrous Membranes with High UV-Resistant Performance by One-Step Electrospinning. *Ind. Eng. Chem. Res.* **2020**, *59* (10), 4447−4458.
(90) Wang, X.; Liu, X.; Li, Z.; Zhang, H.; Yang, Z.; Zhou, H.; Fan, T. Scalable Flexible Hybrid Membranes with Photonic Structures for Daytime Radiative Cooling. *Adv. Funct. Mater.* **2020**, *30* (5), 1907562.
(91) Auvinen, S.; Alatalo, M.; Haario, H.; Vartiainen, E.; Jalava, J.-P.; Lamminmäki, R. J. Refractive Index Functions of TiO2 Nanoparticles. *J. Phys. Chem. C* **2013**, *117* (7), 3503−3512.
(92) Zheng, X.; Xu, B.; Li, S.; Lin, H.; Qiu, L.; Li, D.; Jia, B. Free-Standing Graphene Oxide Mid-Infrared Polarizers. *Nanoscale* **2020**, *12* (21), 11480−11488.
(93) Ergoktas, M. S.; Bakan, G.; Steiner, P.; Bartlam, C.; Malevich, Y.; Ozden-Yenigun, E.; He, G.; Karim, N.; Cataldi, P.; Bissett, M. A.;

https://doi.org/10.1021/acsomega.4c05600
ACS Omega 2024, 9, 49143−49162

Kinloch, I. A.; Novoselov, K. S.; Kocabas, C. Graphene-Enabled Adaptive Infrared Textiles. *Nano Lett.* **2020**, *20* (7), 5346−5352.
(94) Meng, D.; Ma, W.-Z.; Cheng, Y.-Y.; Xu, M.-Y.; Deng, X.-C.; Liu, J.; Chen, Y.-S. Polyethylene Terephthalate-Based Colored Emitters for Efficient Daytime Radiative Cooling. *Results Phys.* **2023**, *46*, 106254.
(95) Liu, Z.; Yang, Y.; Wang, Y.; Gan, X.; Wang, N. Preparation and Properties of Opaque Polyethylene Terephthalate/TiO2 Filaments. *Mater. Sci.* **2021**, *27* (3), 325−329.
(96) Kalaoglu-Altan, O. I.; Kayaoglu, B. K.; Trabzon, L. Improving Thermal Conductivities of Textile Materials by Nanohybrid Approaches. *iScience* **2022**, *25* (3), 103825.
(97) Ma, J.; Zhang, Q.; Mayo, A.; Ni, Z.; Yi, H.; Chen, Y.; Mu, R.; Bellan, L. M.; Li, D. Thermal Conductivity of Electrospun Polyethylene Nanofibers. *Nanoscale* **2015**, *7* (40), 16899−16908.
(98) Wu, G.; Li, J.; Wang, K.; Wang, Y.; Pan, C.; Feng, A. In Situ Synthesis and Preparation of TiO2/Polyimide Composite Containing Phenolphthalein Functional Group. *J. Mater. Sci.: Mater. Electron.* **2017**, *28* (9), 6544−6551.
(99) Nadtochiy, A. B.; Gorb, A. M.; Gorelov, B. M.; Polovina, O. I.; Korotchenkov, O.; Schlosser, V. Model Approach to Thermal Conductivity in Hybrid Graphene−Polymer Nanocomposites. *Molecules* **2023**, *28* (21), 7343.
(100) Mandal, J.; Anand, J.; Mandal, S.; Brewer, J.; Ramachandran, A.; Raman, A. P. Radiative Cooling and Thermoregulation in the Earth's Glow. *Cell Rep. Phys. Sci.* **2024**, *5* (7), 102065.
(101) Xu, J.; Lei, Z.; Liu, S.; Chen, J.; Gong, G.; Cai, X. Preparation and Characterization of Biodegradable Electrospinning PHBV/PBAT/TiO 2 Antibacterial Nanofiber Membranes. *J. Eng. Fibers Fabr.* **2022**, *17*, 155892502211365.
(102) Loaeza, D.; Cailloux, J.; Santana Pérez, O.; Sánchez-Soto, M.; Maspoch, M. Impact of Titanium Dioxide in the Mechanical Recycling of Post-Consumer Polyethylene Terephthalate Bottle Waste: Tensile and Fracture Behavior. *Polymers* **2021**, *13* (2), 310.
(103) Ghasemi, A.; Imani, R.; Yousefzadeh, M.; Bonakdar, S.; Solouk, A.; Fakhrzadeh, H. Studying the Potential Application of Electrospun Polyethylene Terephthalate/Graphene Oxide Nanofibers as Electroconductive Cardiac Patch. *Macromol. Mater. Eng.* **2019**, *304* (8), 1900187.

https://doi.org/10.1021/acsomega.4c05600
ACS Omega 2024, 9, 49143−49162